Author(s): Yim, Jihong; Haimi, Eero; Mäntymäki, Miia; Kärkäs, Ville; Bes, René; Gutierrez, Aitor Arandia; Meinander, Kristoffer; Brüner, Philipp; Grehl, Thomas; Gell, Lars; Viinikainen, Tiia; Honkala, Karoliina; Huotari, Simo; Karinen, Reetta; Putkonen, Matti; Puurunen, Riikka L.

Title: Atomic Layer Deposition of Zinc Oxide on Mesoporous Zirconia Using Zinc(II) Acetylacetonate and Air

Year: 2023

Version: Published version

CHEMISTRY OF MATERIALS

pubs.acs.org/cm

Article

Atomic Layer Deposition of Zinc Oxide on Mesoporous Zirconia Using Zinc(II) Acetylacetonate and Air

Jihong Yim, Eero Haimi, Miia Mäntymäki, Ville Kärkäs, René Bes, Aitor Arandia Gutierrez, Kristoffer Meinander, Philipp Brüner, Thomas Grehl, Lars Gell, Tiia Viinikainen, Karoliina Honkala, Simo Huotari, Reetta Karinen, Matti Putkonen, and Riikka L. Puurunen*

Cite This: https://doi.org/10.1021/acs.chemmater.3c00668

Read Online

ACCESS | Metrics & More | Article Recommendations | Supporting Information

ABSTRACT: The self-terminating chemistry of atomic layer deposition (ALD) ideally enables the growth of homogeneously distributed materials on the atomic scale. This study investigates the ALD of zinc oxide (ZnO) on mesoporous zirconium oxide (ZrO_2) using zinc acetylacetonate [$Zn(acac)_2$] and synthetic air in a fixed-bed powder ALD reactor. A broad variety of methods, including thermogravimetry analysis, scanning electron microscopy with energy-dispersive X-ray spectroscopy, low-energy ion scattering, X-ray absorption near-edge structure, X-ray photoelectron spectroscopy, in-situ diffuse reflectance infrared Fourier transform spectroscopy−mass spectrometry, and density functional theory calculations, were used to analyze the reactant and the resulting samples. The factors affecting the zinc loading (wt %) on ZrO_2 were investigated by varying the ALD reaction temperature (160−240 °C), the calcination temperature of zirconium oxide (400−1000 °C), and the ALD cycle number (up to three). The studied process showed self-terminating behavior with the areal number density of zinc of approximately two atoms per square nanometer per cycle. Zinc was distributed throughout ZrO_2. After the $Zn(acac)_2$ reaction, acac ligands were removed using synthetic air at 500 °C. In the following cycles, already-deposited ZnO acted as nuclei for further ZnO growth. This study demonstrates the potential of $Zn(acac)_2$ as an ALD reactant and provides an initial understanding of ZnO growth via ALD on high surface area porous particles as an example for catalytic applications.

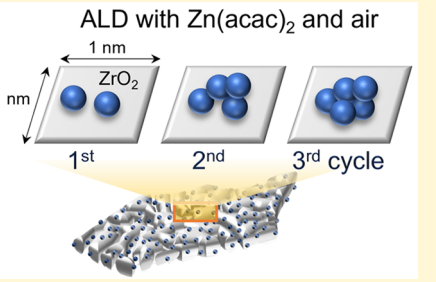

1. INTRODUCTION

The self-terminating chemistry of the atomic layer deposition (ALD) process enables the synthesis of well-defined surface structures. Theoretically, ALD can be used to obtain conformal coatings on high surface area materials, such as porous powders.[1−4] The amount of material deposited can be controlled at an atomic scale by repeating the number of ALD cycles.[5] However, conformality of the ALD process is not self-guaranteed, especially for coatings in high aspect ratio (HAR) features.[1,6−10] Higher exposure is required to saturate the surface of high surface area porous supports compared to coating planar substrates.[6−8,10−16] Various experimental and modeling approaches have been developed to investigate the effect of process parameters on the conformality of ALD with HAR features.[1,6,7,9,10,12,15,17−22] A recent simulation study reported that growth per cycle (GPC) and molar mass of reactant, in addition to the exposure (exposure = partial pressure × reactant pulse time), influence the penetration depth of the ALD coating in a microchannel.[10]

Preparation of heterogeneous catalysts via ALD has attracted increasing global interest, as evident from recent review articles.[23−29] However, the use of ALD for catalysis is not new. ALD has been independently invented two times: as "molecular layering" (ML) in the 1960s by Aleskovskii and Koltsov[30,31] and as "atomic layer epitaxy" (ALE) in 1974 by Suntola.[32,33] Suntola received the Millennium Technology Prize for his invention in 2018.[5] Researchers in both pioneering ALD development branches experimented with catalyst preparation; however, this history has not been well documented in recent review articles. While an exhaustive review of ALD is beyond the scope of this study, the scientific community should be aware of its history. The following paragraph highlights some of the early studies and better-known, more recent studies on ALD-made catalysts.

ALD-made catalysts have been studied in the past 50 years for various applications. Lakomaa et al.[34] summarized the Suntola-related early history of ALE-made catalysts in a book chapter in 2013.[31,35] In the first ALE experiment on porous particles in the late 1980s, elemental zinc was vaporized at 400 °C to react on Zeolite Socony Mobil-5 (ZSM-5).[34] In the following research study, over 40 metal reactants were tested,

Received: March 23, 2023
Revised: September 18, 2023

and scale-up demonstrated up to a 17 kg scale in a circulating fluidized bed for silica−alumina catalysts.[34] Suntola and collaborators patented the apparatus for preparing a heterogeneous catalyst via ALE[36,37] and published reports on, for example, how to control the metal loading via ALE,[4] preparation of nickel-on-alumina catalysts for toluene hydrogenation,[38,39] and preparation of chromia-on-silica catalysts for alkene polymerization.[40] Early studies on ML made catalysts include invention reports on silica modification via sequential adsorption of CrO_2Cl_2 and PCl_3 vapors and water to make catalysts, for example, for dehydrogenation and dehydrocyclization,[41] and $VOCl_3$ and water to make V_2O_5 catalysts for the oxidation of benzol to maleic anhydride.[42] Pioneering investigations on ML (sometimes called "molecular deposition")-made catalysts were also performed by Damyanov and co-workers.[35,43] More recent studies on catalyst preparation via ALD are as follows: the overcoating of Al_2O_3 on palladium nanoparticles via ALD to prevent coking and sintering during the oxidative dehydrogenation of ethane into ethene;[44] addition of Ni nanoparticles on high surface area alumina via ALD to improve hydrogenolysis selectivity compared to that of catalysts made via incipient wetness impregnation method;[45] modification of zeolites, such as ZSM-5,[46,47] and the Pt−SiO_2 interface[48] via ZnO ALD for catalytic applications such as dehydrogenation of propane to propene[47,48] and methanol to aromatics;[46] the modification of V_2O_5 via phosphorus ALD to improve selectivity for oxidation of *n*-butane to maleic anhydride;[49] and the synthesis of TiO_2 on γ-alumina to prepare high surface area titania catalyst supports for hydroprocessing.[50] Recently, Ingale et al.[51] used an extension of ALD, molecular layer deposition, to grow alucone on Ni/SiO_2 catalysts to prevent their deactivation during methane dry reforming. Copper-based catalysts have also been modified via ALD ZrO_2,[52] Ni,[53] and ZnO[54,55] to enhance their catalytic activity and selectivity for the hydrogenation of carbon dioxide to methanol. The well-defined surface structure of ALD-made catalysts provides a better understanding of the relationship between the catalytic performance and structural properties of the ALD-made catalysts.[26,27,45,52−58]

ZnO is a functional material that can be used in various applications, including optical sensors, solar cells, transparent conductive layers, and heterogeneous catalysts.[13,48,59−62] Interestingly, in the works by Suntola and co-workers on ALD-made catalysts, zinc was the first element whose growth on ZSM-5 was attempted via ALD.[34] ZnO can be coated via ALD mostly using diethylzinc (DEZ) and water owing to the good reactivity and high vapor pressure of DEZ.[13,14,47,62] However, DEZ is pyrophoric and environmentally hazardous.[63] Additionally, a study reported the decomposition of DEZ at a temperature above 80 °C.[14] Other ALD reactants and oxygen sources, such as Zn and water,[64] Zn and O_2,[65] zinc acetate [$Zn(OAc)_2$] and water,[66−68] dimethylzinc [$Zn(CH_3)_2$] and water,[46,69,70] zinc chloride ($ZnCl_2$) and water,[71] $ZnCl_2$ and O_2,[65,72,73] and DEZ and O_2 plasma,[74] have been reported for ZnO ALD.

To the best our knowledge, zinc acetylacetonate [$Zn(acac)_2$] has not been reported as a zinc source in experimental ALD studies, although it has been suggested in a computational study.[75] $Zn(acac)_2$ is nontoxic and stable in air, has a relatively low vapor pressure compared to DEZ, and exists as a solid at normal temperature and pressure.[14,76] In a recent study, $Zn(acac)_2$ was used as a preferential chemical vapor deposition reactant to promote the Cu/Al_2O_3 catalyst for hydrogenation of carbon dioxide to methanol.[58] In another study, a ZnO film was grown via CVD using $Zn(acac)_2$ and O_3.[77] A recent study by Arandia et al.,[55] related to the current study, reported the beneficial effect of adding ZnO after copper impregnation on catalytic performance for hydrogenation of carbon dioxide to methanol. The study by Arandia et al.[55] used $Zn(acac)_2$ and synthetic air to deposit ZnO via ALD, which is explored in more detail in this study.

This study aimed to demonstrate the potential of $Zn(acac)_2$ as an ALD reactant, especially for modifying the surface of mesoporous supports. Mesoporous zirconium oxide (ZrO_2) supports were treated with $Zn(acac)_2$ in a fixed-bed powder ALD reactor. The suitability of $Zn(acac)_2$ as an ALD reactant was investigated via thermogravimetric (TG) analysis, and the saturating nature of the $Zn(acac)_2$ reaction under our reaction conditions was also investigated. Additionally, the effects of the ALD reaction temperature, calcination temperature, and number of ALD cycles on zinc loading were also investigated. Scanning electron microscopy (SEM) with energy-dispersive X-ray spectrometry (EDS), inductively coupled plasma−optical emission spectrometry (ICP-OES), carbon content analysis, in-situ diffuse reflectance infrared Fourier transform spectroscopy−mass spectrometry (DRIFTS-MS), DFT calculations, X-ray absorption near-edge structure (XANES) analysis, X-ray photoelectron spectroscopy (XPS), and low-energy ion scattering (LEIS) were used to obtain Information on the deposited zinc and surface species.

2. EXPERIMENTAL SECTION

2.1. Materials. A mesoporous monoclinic zirconium oxide powder (ZrO_2, Saint-Gobain, 99.0%, grinded and sieved particle size of 250−420 μm) was used as a support for ALD. ZrO_2 was calcined in synthetic air (99.999%, Oy AGA Ab) typically at 600 °C for 5 h at a heating rate of 5 °C/min. To study the effect of the calcination temperature on zinc loading, ZrO_2 was calcined at various temperatures of 400, 600, 800, and 1000 °C.

$Zn(acac)_2$ (Volatec, 99.99%) and synthetic air (99.999%, Oy AGA Ab) were used as the ALD reactants. Acetylacetone (Hacac, 2,4-pentanedione, Merck, >99%) was used to prepare Hacac bound to ZrO_2 (sample labeled Hacac/ZrO_2) for comparative purposes. Nitrogen (N_2) generated from air (<10 ppm of oxygen) using a Parker HPN2-5000 high-purity nitrogen generator was used as carrier and purge gases.

2.2. Nitrogen Physisorption. The physical properties of ZrO_2 calcined at different temperatures and samples prepared with different ALD cycles were analyzed via nitrogen physisorption (77 K, liquid nitrogen) using a Thermo Scientific SURFER. Before measurements, around 200 mg of the sample was degassed at 180 °C for 2 h. The quantity of adsorbed nitrogen was given under the standard temperature and pressure conditions (STP). From the physisorption isotherm (Figure S1a), the specific surface area and Barrett−Joyner−Halenda (BJH) pore size distribution (Figure S1b) were calculated using the Brunauer−Emmett−Teller (BET) method[78] and the BJH method,[79] respectively. The specific surface area, total pore volume, and median pore diameter of calcined ZrO_2 are given in Table 1.

2.3. Thermal Analysis of the Zn(acac)$_2$ Reactant. The TG analysis of $Zn(acac)_2$ was performed by using a Netzsch STA 449F3 Jupiter simultaneous thermal analyzer. $Zn(acac)_2$ was heated in a flowing nitrogen atmosphere (40 mL/min) at ambient pressure from room temperature to 600 °C. The heating rate was 10 °C/min. The mass of the sample in the 90 μL pan was approximately 10 mg. Samples were measured with and without a lid. Using a lid with a small orifice slows down the evaporation of the sample, thus making any decomposition more visible in the resulting TG curve.

2.4. Chemisorption of Zn(acac)$_2$ on ZrO$_2$. The reaction of $Zn(acac)_2$ with mesoporous ZrO_2, typically at 200 °C, was performed

https://doi.org/10.1021/acs.chemmater.3c00668
Chem. Mater. XXXX, XXX, XXX−XXX

Table 1. BET Surface Area, Cumulative Pore Volume, and Median Pore Diameter of ZrO_2 Calcined at Varied Temperatures Analyzed Using N_2 Physisorption Measurements

calcination temp (°C)	BET surf. area ($m^2\ g^{-1}$)	total pore vol ($cm^3\ g^{-1}$)	median pore diam (nm)
400	99.2	0.34	9.8
600	53.5	0.26	16.6
800	28.6	0.19	26.0
1000	14.5	0.033	8.0

in a flow-type ALD reactor (F-120, ASM Microchemistry Ltd., Finland) equipped with a powder chamber (Figure S2). Typically, after preheating ZrO_2 with N_2 at 250 °C for 10 h in the reactor, 2 g of calcined ZrO_2 was used as a support. Typically, 1.9 mmol of $Zn(acac)_2$ per gram of ZrO_2 was sublimed at 120 °C and ca. 5 mbar, and the reactant vapor was carried by N_2 (the 100 sccm of inlet N_2 flow was divided into six different inlet tubes within the reactor). To ensure the saturation of the reaction with ZrO_2, a sufficient pulse time of 3 h was used with different dose of $Zn(acac)_2$ [0.2, 0.5, 1.0, and 1.9 mmol $Zn(acac)_2$ per gram of ZrO_2 by placing 0.0625, 0.125, 0.25, and 0.5 g of $Zn(acac)_2$ per gram of ZrO_2 into the reactor, respectively]. Leftover reactants and byproducts were purged for 2 h, followed by cooling in N_2 at approximately room temperature. After the reaction, sampling was performed twice by tilting the powder bed. (Samples **a** and **b** were mostly collected from the top and bottom parts of the powder bed, respectively.) For the samples prepared with 1.0 mmol of $Zn(acac)_2$ per gram of ZrO_2, the experiment was repeated five times (an average sample was taken after mixing the powder and denoted by "Repeat"). To study the effect of ALD temperature on zinc loading on ZrO_2, the deposition temperature was varied as follows: 160, 180, 200, 220, and 240 °C. To study the effect of the calcination temperature of ZrO_2 on zinc loading, the ZrO_2 powder calcined at various temperatures was used as a support. Herein, one full reaction cycle includes the reaction of $Zn(acac)_2$ with ZrO_2, followed by purging for 2 h with N_2 in the ALD reactor and the removal of acetylacetonate (acac) ligands via oxidative treatment at 500 °C for 2 h (5 K/min) in a tube furnace in synthetic air (100 mL/min) (Figure S3). The zinc loading on ZrO_2 was controlled by repeating the number of reaction cycles up to three. These samples with two or three ALD cycles were prepared from the same batch. For a comparison, a Hacac/ZrO_2 sample was prepared via ALD. Hacac was evaporated at 55 °C and reacted with ZrO_2 at 200 °C for 3 h in the reactor followed by purging for 2 h and cooling to room temperature in N_2.

2.5. Characterization. The zinc loading on the sample was analyzed via ICP-OES. Approximately 100 mg of the sample weighed in a Teflon vessel was dissolved in a mixture of nitric acid (HNO_3, 65%, 2.5 mL) and hydrochloric acid (HCl, 37%, 7.5 mL) by heating it at 200 °C for 1 h in a microwave oven (Milestone, Ethos) and cooling it to room temperature. The dissolved sample was diluted by using Milli-Q-grade water. The zinc loading on the sample was determined using an F-AAS instrument (Varian 220 F) with an air−acetylene burner.

The zinc distribution within several ZrO_2 particles was analyzed via cross-sectional SEM-EDS. The sample, which was stored in ambient air, was vacuum-impregnated in epoxy resin, and its cross section was revealed by manual target polishing. The polished sample was carbon-coated using a LEICA EM SCD050 to prevent charging under the electron beam. SEM-EDS was performed using a Tescan Mira3 SEM fitted with a Thermo Scientific EDS. The EDS line scan was measured at an accelerating voltage of 15 keV. Irrespective of variation in particle cutting planes, similar results were attained. One representative image was selected to be discussed further in this work.

The crystalline phase of ZrO_2 calcined at an elevated temperature of 1000 °C was analyzed via powder X-ray diffraction (XRD) using a PANanalytical X'Pert Pro MPD Alpha 1 device with Cu Kα radiation. A X-ray scanning range from 5 to 100° (2θ), a step size of 0.026°, and a time per step of 99.45 s were applied.

The carbon content of the $Zn(acac)_2/ZrO_2$ and nonmodified ZrO_2 reference was determined using a FlashSmart elemental analyzer. The sample was weighed in a tin container and introduced into the combustion reactor using a MAS Plus Autosampler with 250 mL/min of oxygen. After combustion up to 950 °C the evolved gases were carried by 140 mL/min of a helium flow to a copper-filled layer, swept through a gas chromatography column that separated the combustion gases, and finally detected using a thermal conductivity detector.

XANES spectra were acquired using the laboratory-scale XANES instrument Hel-XAS at the University of Helsinki Center for X-ray Spectroscopy.[80] Briefly, the instrument is based on a spherically bent Ge(555) crystal monochromator using Johann geometry with a curvature radius (Rowland circle diameter) of 0.5 m. The X-ray source was a water-cooled X-ray tube (XRD Eigenmann), and the detector was a silicon drift diode (Amptek X-123SDD). Approximately 10 mg of each powder sample was mixed with a buffer material (starch) to make 2 mm thick pellets for transmission XANES.

The surface composition of the samples was studied via XPS using a Kratos AXIS Ultra DLD spectrometer with a monochromated Al Kα X-ray source (1486.7 eV). The base pressure of the system was typically below 1×10^{-9} Torr. During measurements the source was run at a power of 100 W, and photoelectrons were collected at a 90° takeoff angle, with a pass energy of 80 eV and a step size of 1.0 eV for survey spectra and a pass energy of 20 eV and a step size of 0.1 eV for high-resolution spectra. All spectra were charge-corrected relative to the position of the C−C bonding of adventitious carbon at 284.8 eV. The homogeneity of the samples was confirmed by collecting spectra from three separate spots on the surface of each sample, and results from all three spots were used to calculate average values for elemental concentrations.

LEIS measurements were used to analyze the elemental composition of the first atomic layer of the sample. The measurements were performed at IONTOF GmbH (Münster, Germany) by using a Qtac100 LEIS spectrometer. The instrument is equipped with a double toroidal electrostatic analyzer simultaneously optimized for maximum sensitivity and high mass resolution. The analysis ion beam hits the sample surface at normal incidence, and all ions scattered at a 145° angle are transmitted to the energy analyzer. The samples were compacted into flat pellets for introduction into the vacuum system of the instrument. Before LEIS analysis, the samples were cleaned by exposure to atomic oxygen extracted from oxygen plasma. This cleaning procedure removes all atmospheric contaminants and completely oxidizes the surface of the sample. $^4He^+$ and $^{20}Ne^+$ primary ions were used for the analysis, with a $2 \times 2\ mm^2$ analysis field of view. The analysis ion dose density was limited to 5×10^{13} and 1×10^{13} ions/cm^2 for He and Ne ions, respectively. This ensures that the analysis stays below the static limit; that is, the top atomic layer is not significantly altered by ion beam damage during analysis.

2.6. Temperature-Controlled Oxidation of Acac Ligands. The oxidation of the acac ligands remaining on $Zn(acac)_2/ZrO_2$ samples prepared at ALD temperatures of 200 and 240 °C was observed via in-situ DRIFTS-MS. DRIFTS was measured by using a Nicolet Nexus FTIR spectrometer and a high-temperature Spectra-Tech reactor chamber with a deuterated triglycine sulfate detector. The DRIFTS setup was coupled with a mass spectrometer (OmniStar GSD 301 by Pfeiffer Vacuum) with a faraday cup detector. 100 scans were collected in the wavenumber of ranging from 4000 to 600 cm^{-1} at a scan resolution of 4 cm^{-1}. Before the experiment, a background spectrum was measured using an aluminum mirror (scan resolution of 4 cm^{-1}, 200 scans) under an Ar flow (99.999%, Woikoski). The DRIFT spectra of Hacac/ZrO_2, ZrO_2, and $Zn(acac)_2$ were measured as references. The DRIFT spectrum of the $Zn(acac)_2$ reference was measured at 30 °C with 50 mL/min Ar (99.999%, Woikoski). $Zn(acac)_2/ZrO_2$, ZrO_2, and Hacac/ZrO_2 references were placed in an in-situ cell and heated from 30 to 180 °C for 2 h with 50 mL/min of Ar (99.999%, Woikoski) and at a heating step of 15 °C (Figure S5). The heating process was followed by cooling to 30 °C with Ar. DRIFT spectra were recorded at 30 and 180 °C (0, 60, and 115 min)

https://doi.org/10.1021/acs.chemmater.3c00668
Chem. Mater. XXXX, XXX, XXX−XXX

and after cooling. Next, the oxidative removal of acac ligands from the $Zn(acac)_2/ZrO_2$ sample was performed by heating the sample up to 500 °C (heating in steps of 5 °C) in synthetic air (25 mL/min synthetic air mixed with 25 mL/min Ar) and keeping the sample at 500 °C for 30 min. The oxidation step was followed by cooling to 30 °C in 50 mL/min of Ar. DRIFT spectra were recorded every 25 °C during heating, at 500 °C, and at 500 °C after 30 min. The DRIFT spectra were obtained as % reflectance and converted to Kubelka–Munk units using the following equation:[81]

$$f(R) = \frac{(1-R)^2}{2R} = \frac{k}{s} \quad (1)$$

where R is the diffuse reflectance, k is the absorption coefficient of the sample, and s is the scattering coefficient.[81]

2.7. Areal Number Density Calculation. The areal number density of metal c_M (nm^{-2}) represents how many metal atoms (herein, zinc) are deposited per unit surface area,[5] obtained as follows (eq 25 in ref 82):

$$c_M = \frac{w_M N_A m_t}{M_M S m_s} \quad (2)$$

Here, W_M is the metal weight fraction (−), N_A is Avogadro's number (mol^{-1}), M_M (g_{metal} mol^{-1}) is the molar mass of metal M, S (m^2 $g_{support}^{-1}$) is the specific surface area of the support, m_t (g_{sample}) is the total mass of the sample including the amount of the deposited material, and m_s ($g_{support}$) is the mass of the original support. This calculation assumes that the mass of ZnO is added to the sample after the $Zn(acac)_2$ reaction without affecting the total surface area of the sample (m^2). (After each ALD cycle, the specific surface area expressed as m^2/g decreases because of the mass gain.[82]) The mass of oxygen deposited on the sample was determined assuming a 1:1 stoichiometry of MO (M = Zn). Note that areal number density counts all metal atoms added via ALD, and it does not reveal how individual species are arranged (e.g., how many metal atoms are on the outermost surface).[5]

The GPC expressed as the areal number density of metal Δc_M (nm^{-2}) can be calculated from the GPC in thickness increment Δh (nm) as follows (eq 12 in ref 83):

$$\Delta h = \frac{M}{\rho N_A} \Delta c_M \quad (3)$$

Here, ρ ($g\ m^{-3}$) is the mass density of the MZ_x material, and M ($g\ mol^{-1}$) is the molar mass of one unit of MZ_x.

For an average bulk monolayer of the MZ_x material,[5] the areal number density of metal can be obtained as follows (eq 16 in ref 83):

$$\bar{c}_M^{ml} = \left(\frac{\rho N_A}{M}\right)^{2/3} \quad (4)$$

2.8. Computational Methods. DFT calculations were performed using the projector-augmented wave (PAW)[84] formalism as implemented in the grid-based PAW (GPAW) package.[85] The Bayesian error estimation functional (BEEF)–vdW exchange–correlation functional[86] was assumed, and the core electrons of all elements were described by PAW setups in the frozen-core approximation. A maximum spacing of 0.20 Å was used for the real-space grid basis, and the reciprocal space was sampled at 2 × 2 × 1 k-points for structure optimization and at 16 × 16 × 1 k-points for IR frequency calculations. We applied a Hubbard U correction[87,88] of 2.0 eV to the d-orbitals of zirconium atoms. Geometry optimizations were performed using the Fast Inertial Relaxation Engine algorithm as implemented in the Atomic Simulation Environment.[89,90] IR frequencies were calculated using the Frederiksen method.[91]

A monoclinic ZrO_2 (−111) surface was modeled with a 1 × 1 × 2 unit cell and periodic boundary conditions in x and y directions together with a 6 Å vacuum on the top and bottom of the surface. The computational cell measures 6.9 × 7.4 × 25.9 $Å^3$ with angles of 90° × 90° × 116.5°, resulting in a surface area of 0.455 nm^2. During geometry optimization, the two bottom layers of the ZrO_2 slab were kept frozen in its initial bulk geometry while all other atoms were allowed to relax until the maximum residual force was reduced below 0.005 eV $Å^{-1}$. To understand the impact of ZnO ALD on the structure and IR spectrum of the ZrO_2 surface, a monoclinic ZrO_2 (−111) surface covered with adsorbed water was compared to a surface with ZnO and adsorbed water. One ZnO per computational unit cell was considered, which corresponds to an experimentally measured areal number density of ZnO of 2.2 nm^{-2} after one ALD cycle. We also considered two distinct water concentrations on the surface: (a) two water molecules per unit cell (areal number density 4.4 OH/nm^2) and (b) three water molecules per unit cell (areal number density 6.6 OH/nm^2).

3. RESULTS

3.1. Thermal Analysis of $Zn(acac)_2$. The behavior of the $Zn(acac)_2$ reactant during heating was observed via TG analysis. The sample was measured without and with a lid on the top of the sample at atmospheric pressure under a N_2 flow. The lid with a small orifice made any decomposition more visible. Figure 1 shows the $Zn(acac)_2$ mass remaining versus

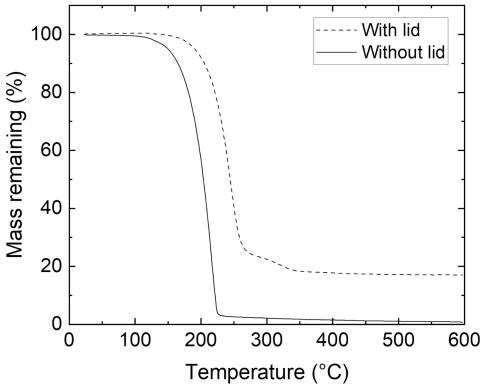

Figure 1. TG analysis of $Zn(acac)_2$ under a N_2 flow (40 mL/min) at ambient pressure from room temperature to 600 °C. The heating rate was 10 °C/min. The sample was heated without (solid line) and with a lid (dashed line).

temperature [differential scanning calorimetry (DSG) and derivative thermogravimetric (DTG) curves were depicted in Figure S4]. The $Zn(acac)_2$ reactant evaporated with only a small residue until about 200–220 °C when heated without a lid (solid line, Figure 1). When the reactant was heated with a lid, some decomposition was observed above 275 °C (dashed line, Figure 1). Therefore, the highest deposition temperature was limited below 250 °C. Based on the weight loss onset observed, a sublimation temperature of 120 °C was selected for ALD experiments.

3.2. Chemisorption of $Zn(acac)_2$ on ZrO_2. To investigate the ZrO_2 surface saturation with the $Zn(acac)_2$ reaction, the amount of the $Zn(acac)_2$ reactant sublimed per gram of ZrO_2 was varied. Figure 2 shows the zinc loading (wt %) and zinc areal number density (nm^{-2}) versus the amount of $Zn(acac)_2$ sublimed. Samples **a** and **b** were collected mostly from the top and bottom parts of the bed, respectively. With a low amount of $Zn(acac)_2$, the zinc loading on sample **b** is significantly lower than that on sample **a**, indicating that the reactant dose is not sufficient to saturate the surface throughout the powder bed. When the amount of $Zn(acac)_2$ increases, the zinc loading on ZrO_2 settles to an almost constant value of ca. 2.2 nm^{-2}. Concurrently, the zinc loading from sample **b** is close to that of sample **a**. These results

https://doi.org/10.1021/acs.chemmater.3c00668
Chem. Mater. XXXX, XXX, XXX–XXX

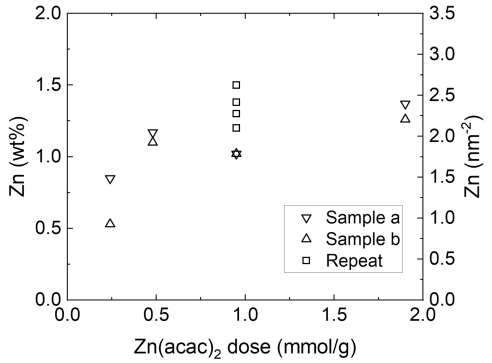

Figure 2. ICP-OES analysis of the zinc loading on ZrO_2 as a function of the $Zn(acac)_2$ dose. An ALD temperature of 200 °C was used. The areal number density of zinc (nm^{-2}) was calculated by using a specific surface area of calcined ZrO_2 of 53.5 m^2 g^{-1}.

indicate that the reaction of $Zn(acac)_2$ on ZrO_2 is a self-terminating process[1] that can be used in an ALD process under our reaction conditions.

The $Zn(acac)_2$ process under conditions typically used in this study [1.0 mmol of $Zn(acac)_2$ per gram of ZrO_2, ALD temperature = 200 °C] was tested five times to investigate the repeatability among different ALD runs. For most of these samples, sampling was performed once (marked as "Repeat" in Figure 2). Different runs showed somewhat different zinc loadings (average of six observations = 1.2 wt %, standard deviation = 0.19 wt %, relative standard deviation = 15.8%). Small differences in the surface area of ZrO_2 calcined in different batches and uncertainty in ICP-OES measurement (relative standard deviation <5%) are likely the sources for the difference in zinc loadings.

3.3. Distribution of Zinc within a ZrO_2 Particle. The presence of Zn within several ZrO_2 particles was observed via EDS analysis. Figure 3a illustrates the position of the EDS line scan on top of the backscattered electron image of a particle, and Figure 3b shows the X-ray intensities of Zn and Hf along the line scan. Hf is an evenly distributed impurity in ZrO_2, and it serves as a reference. The measured X-ray intensities are proportional to the concentrations of Zn and Hf, respectively. Therefore, Zn was present throughout the ZrO_2 particle. However, less Zn is present in the central part of the particle compared to that on the outermost surface.

3.4. Effect of ALD Temperature and Calcination Temperature on Zinc Loading. The effect of the ALD temperature on the zinc loading was investigated. Figure 4 shows the zinc loading versus ALD temperature (160−240 °C). [The data marked as "Repeat" is already discussed in Subsection 3.2, and the spread was discussed there.] The zinc loading is almost constant up to an ALD temperature of 200 °C. Above 200 °C, a slight increase in zinc loading is observed with an increase in the ALD temperature.

To investigate the effect of the support calcination temperature on zinc loading, the ALD reaction at 200 °C was performed on ZrO_2 calcined at various temperatures from 400 to 1000 °C. Figure 5 shows the zinc loading and specific surface area of ZrO_2 versus the calcination temperature. Both the zinc loading and the specific surface area of ZrO_2 decrease with an increase in ZrO_2 calcination temperature. Interestingly, the zinc areal number density (nm^{-2}) is almost constant as ca. 2 nm^{-2} with an increase in the calcination temperature. After

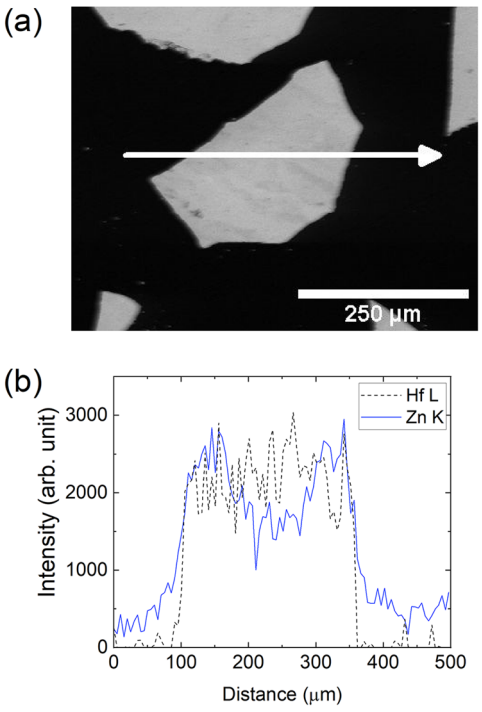

Figure 3. Zinc distribution in a $Zn(acac)_2/ZrO_2$ sample [1.0 mmol of $Zn(acac)_2$ per gram of ZrO_2] analyzed via SEM-EDS. (a) Back-scattered electron image showing the location of EDS line scan. (b) EDS line scans showing the intensity of zinc relative to that of hafnium in ZrO_2.

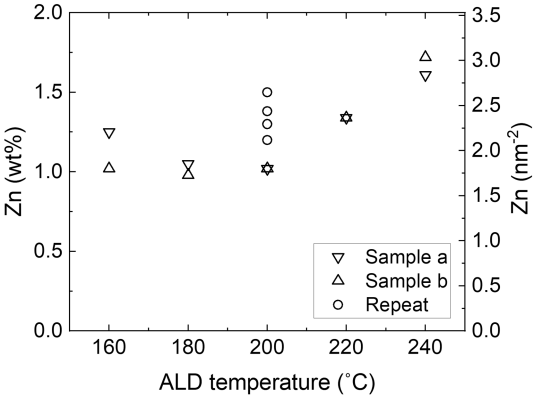

Figure 4. Zinc loading on the $Zn(acac)_2/ZrO_2$ samples vs ALD temperatures. The areal number density of zinc (nm^{-2}) was calculated by using the BET surface area of ZrO_2 (53.5 m^2 g^{-1}) calcined at 600 °C. A $Zn(acac)_2$ dose of 1.0 mmol per gram of ZrO_2 was used.

calcination at 1000 °C, the crystalline phase of ZrO_2 is still monoclinic, as observed via XRD (Figure S9).

3.5. Temperature-Controlled Oxidation of Acac Ligands. After the chemisorption of $Zn(acac)_2$ on ZrO_2 (the first step in the ALD cycle[5]), some acac ligands were attached on the sample surface. These remaining ligands were removed before the next ALD cycle, via thermal oxidation. The surface species after the $Zn(acac)_2$ reaction with ZrO_2 and the removal of remaining ligands via thermal oxidation in synthetic air were investigated via in-situ DRIFTS-MS.

Figure 6 shows the in-situ DRIFT spectra of $Zn(acac)_2/ZrO_2$ prepared at 200 and 240 °C and those for $Zn(acac)_2$, $Hacac/ZrO_2$, and bare ZrO_2 for comparison. Before oxidative

https://doi.org/10.1021/acs.chemmater.3c00668
Chem. Mater. XXXX, XXX, XXX−XXX

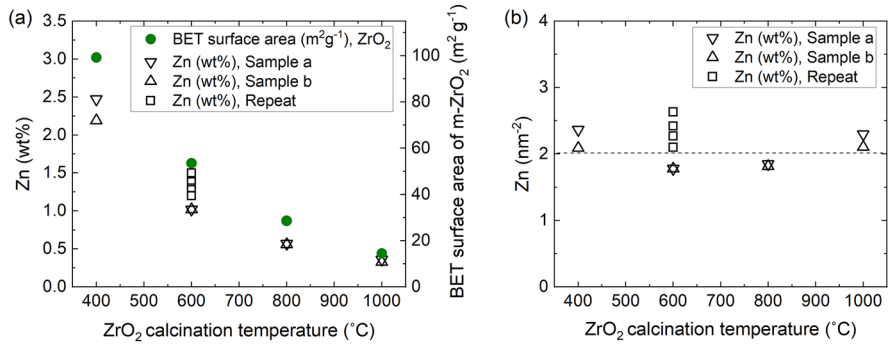

Figure 5. Zinc loading on $Zn(acac)_2/ZrO_2$ as a function of the ZrO_2 calcination temperature. The $Zn(acac)_2$ reaction temperature was 200 °C. (a) Specific surface area of ZrO_2 and zinc loading versus calcination temperature. (b) Areal number density of zinc (nm^{-2}) versus calcination temperature. A $Zn(acac)_2$ dose of 1.0 mmol per gram of ZrO_2 was used, unless stated otherwise.

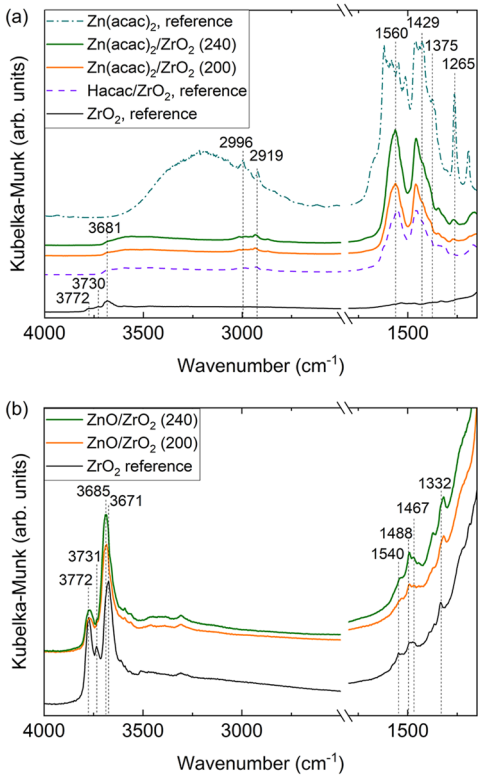

Figure 6. DRIFT spectra of $Zn(acac)_2/ZrO_2$ samples prepared at different ALD temperatures (ALD temperature in parentheses) (a) before and (b) after oxidative removal of acac ligands at 500 °C in synthetic air followed by cooling to 30 °C with Ar. The spectra of bare ZrO_2, Hacac/ZrO_2, and $Zn(acac)_2$ reactant are shown as a reference in (a).

removal of acac ligands, DRIFT spectra were measured at 30 °C in the presence of Ar and after the pretreatment at 180 °C with Ar. The DRIFT spectrum of bare ZrO_2 exhibits three bands at 3772, 3730, and 3681 cm^{-1}, corresponding to different kinds of ν(OH) (terminal, bibridged, and tribridged hydroxyl groups, respectively).[92,93] After $Zn(acac)_2$ reactions with ZrO_2 at different temperatures, the first two bands at 3772 and 3730 cm^{-1} disappear. The DRIFT spectra of $Zn(acac)_2/ZrO_2$ and Hacac/ZrO_2 exhibit a broad band at 3550−3500 cm^{-1}, which can be assigned to hydrogen-bonded hydroxyl group.[92,94,95] This broad band was not observed in the DRIFT spectrum of ZrO_2.

The $Zn(acac)_2$ and Hacac/ZrO_2 reference DRIFT spectra exhibit bands at ca. 3000−2910, 1560, 1429, 1375, and 1265 cm^{-1}. The bands at ca. 3000−2910 cm^{-1} can be assigned to ν(C−H) of methyl groups.[38] The bands at ca. 1560, 1375, and 1265 cm^{-1} can be assigned to ν_s(C═O), ν_{as}(C═O), and ν_s(C═C) from acac ligands, respectively.[94,96,97] The band at 1429 cm^{-1} is mostly from δ(C−H) from acac ligands.[96] Similar bands, especially in the fingerprint region, are observed in the DRIFT spectra of the $Zn(acac)_2/ZrO_2$ samples, indicating the presence of acac ligands in prepared samples. The DRIFT spectrum of the sample prepared at the ALD temperature of 240 °C is similar to that of the sample prepared at the ALD temperature of 200 °C with higher peak intensities near 1560 and 1429 cm^{-1}.

The carbon content of the $Zn(acac)_2/ZrO_2$ sample was determined after the $Zn(acac)_2$ reaction with ZrO_2 at 200 °C. The carbon content in the $Zn(acac)_2/ZrO_2$ sample was 0.96 wt %. For comparison, the carbon content measured for the nonmodified ZrO_2 reference was almost negligible as 0.12 wt %. The areal number density of the acac ligand was calculated from the measured carbon content and specific surface area of 53.5 $m^2\ g^{-1}$. Around 1.8 nm^{-2} of the acac ligand was bound to the $Zn(acac)_2/ZrO_2$ sample.

Figure 7 shows the DRIFT spectrum of $Zn(acac)_2/ZrO_2$ prepared at 200 °C during oxidative removal of the remaining acac ligands in synthetic air at an elevated temperature. Figure 7a shows a band at about 3670 cm^{-1}, which can be attributed to ν(OH). In Figures 7b and 7c, bands at ca. 2950, 1700, 1550, and 1450 cm^{-1} can be attributed to ν(C−H) of the methyl group, combined ν(C═C) and ν(C═O) of the conjugated chelate ring, and δ(C−H), respectively.[94,98] The intensity of these peaks decreases with an increase in temperature, indicating the removal of acac ligands. A broad band (3550−3500 cm^{-1}) in the DRIFT spectra measured at 300 °C can be from strongly hydrogen-bonded OH groups, and the intensity of this band decreases with an increase in temperature.[92,94,99] During oxidation of remaining acac ligands, the intensity of the band at 3670 cm^{-1} increases with increasing oxidation temperature up to 500 °C, as shown in Figure 7a, indicating the formation of new surface hydroxyl groups.[56] MS analysis supports the results of DRIFTS. Figure 7 shows the oxidation product monitored via MS against the treatment time and temperature. The signal for the mass/charge ratio of m/z = 44, which is most likely from CO_2, is observed from below 100 °C, and the intensity increases at approximately 250 °C. The signal intensity decreases to almost 0 at around 450 °C, suggesting

https://doi.org/10.1021/acs.chemmater.3c00668
Chem. Mater. XXXX, XXX, XXX−XXX

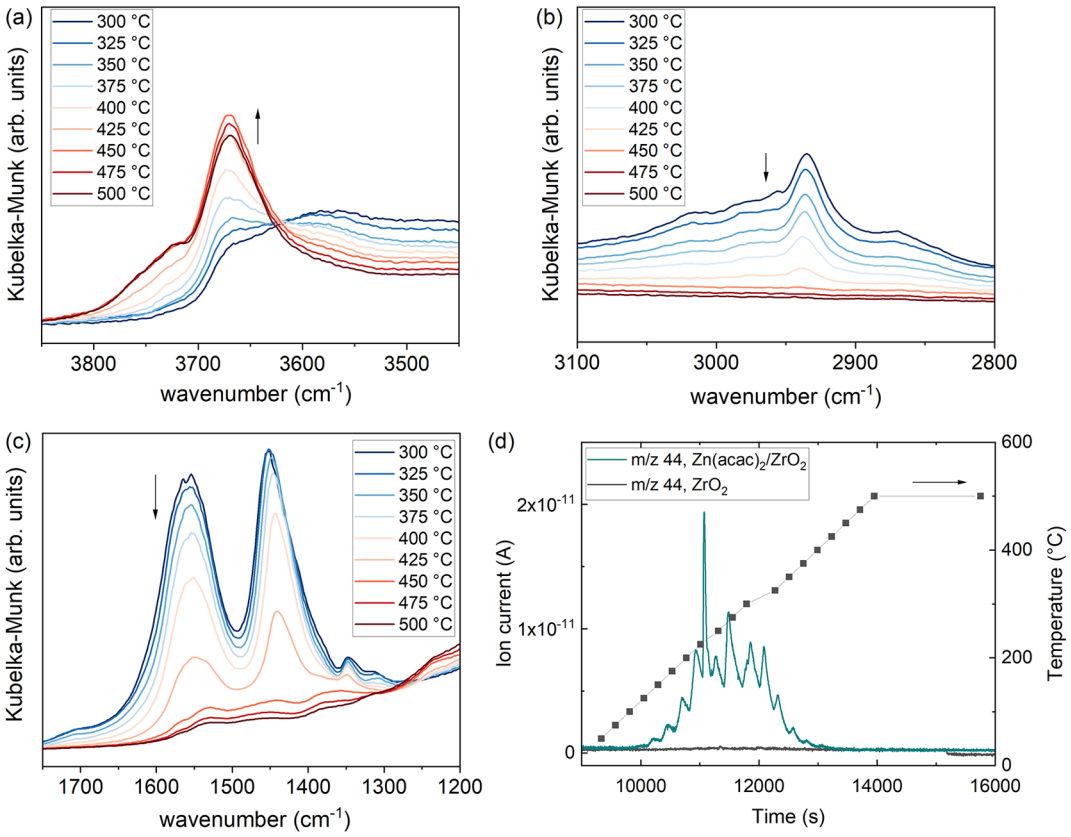

Figure 7. In-situ DRIFT spectra (a–c) of $Zn(acac)_2$-modified ZrO_2 at 200 °C during the oxidation of acac ligands from 300 to 500 °C in synthetic air (the arrow indicates the direction of increasing temperature). (d) Mass spectra of $Zn(acac)_2$-modified ZrO_2 and pure ZrO_2 during the same treatment as (a–c).

that all acac ligands on the samples are removed above this temperature. The mass spectrum of the ZrO_2 reference was also recorded while heating, and no signal for m/z = 44 was observed.

After the thermal oxidation of acac ligands in synthetic air, the samples were cooled to 30 °C with Ar. Figure 6b exhibits in-situ DRIFT spectra of samples prepared at different ALD temperatures (200 and 240 °C) and calcined ZrO_2 as a reference after the cooling process. The DRIFT spectrum of ZrO_2 exhibits bands at 3772, 3731, and 3671 cm^{-1}, which can be attributed to terminal, bibridged, and tribridged ν(OH), respectively.[92,93] When ZnO is deposited on ZrO_2, the intensity of the bands at 3772 and 3731 cm^{-1} decreases, indicating that $Zn(acac)_2$ reacts with some of the terminal and bibridged hydroxyl groups on ZrO_2. In the DRIFT spectrum of ZnO/ZrO_2, a peak shift is observed from 3671 to 3685 cm^{-1}, compared to those of ZrO_2, while the peak intensity is almost similar. Small bands are observed in the region of ca. 1330–1550 cm^{-1}. These bands correspond to bidentate (1540 and 1330 cm^{-1}) and monodentate (1488 cm^{-1}) carbonate and bicarbonate (1467 cm^{-1}) species.[100] These species may be formed by CO_2 produced during the decomposition of acac ligands; however, these bands are also observed in the DRIFT spectrum of bare ZrO_2.

After each reaction of $Zn(acac)_2$ with the support in the ALD reactor, the sample was calcined in a tube furnace to remove acac ligands and stored in a desiccator before the next reaction. The DRIFT spectrum of the calcined ZnO/ZrO_2 sample (ALD cycle number of one) exhibits bands at ca. 1500 cm^{-1}, corresponding to bicarbonates and carbonates, indicating the presence of adsorbed CO_2 on the surface (Figure S6).[93]

3.6. DFT Calculations of Different Bands of Hydroxyl Group. The effect of ZnO ALD on the structure and IR spectrum of the ZrO_2 surface was investigated via DFT calculations. Figure 8 shows the minimum-energy structures for all of the studied systems. In the case of two water molecules, Figure 8a shows that the adsorption is dissociative,

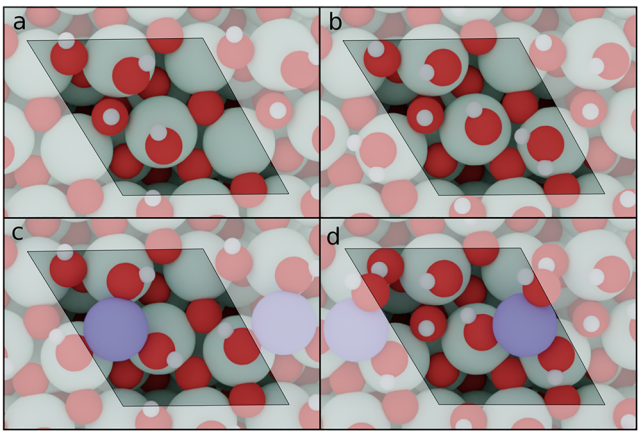

Figure 8. Obtained minimum-energy structures for (a) two H_2O molecules, (b) three H_2O molecules, (c) one ZnO and two H_2O molecules, and (d) one ZnO and three H_2O molecules adsorbed on a monoclinic ZrO_2 (−111) surface. Colors: O, H, Zr, and Zn are colored red, white, light green, and blue, respectively.

https://doi.org/10.1021/acs.chemmater.3c00668
Chem. Mater. XXXX, XXX, XXX−XXX

with hydroxyl groups occupying Zr-top positions and the hydrogen atoms sitting on two- and three-coordinated oxygen anions. Figure 8b shows that the third water molecule adsorbs molecularly to a Zr cation via oxygen. Both water adsorption structures well agree with the previously computed adsorption structures on ZrO_2 (−111).[101]

When ZnO is added on the surface having two dissociated water molecules, the Zn atom replaces hydrogen that was previously bound to the three-coordinated oxygen of ZrO_2. This hydrogen atom is instead attached to oxygen in the ZnO species. Figure 8c shows that ZnO addition leads to surface-bound $Zn(OH)_3$ with each OH group sitting in a Zr-top position. Figure 8 shows that the presence of three water molecules on the surface also results in the formation of a $Zn(OH)_3$ complex, but the Zn atom and one hydroxyl group are slightly farther away from the surface than the other two hydroxyls, which reside over Zr cations. Analyzing adsorption energies of water, we find that the dissociative adsorption energy of two water molecules on bare ZrO_2 is exothermic by −2.11 eV (or −1.05 eV on average per water molecule), whereas that on the ZnO-modified surface adsorption is exothermic by −3.39 eV (or −1.69 eV on average per water molecule) owing to the formation of the Zn complex. In addition, the adsorption of a third water molecule on the ZnO-modified zirconia is endothermic by 0.35 eV, whereas on ZrO_2, the adsorption is exothermic by −1.03 eV.

O−H IR frequencies of the surfaces for each surface structure were calculated together with the corresponding OH binding environment (Table S1). For the two−water molecule system, we identify four bands (at 3872, 3831, 3733, and 3688 cm^{-1}) with the highest two frequencies standing for the hydroxyl group on a Zr-top position and the lowest two frequencies representing two- and three-coordinated lattice −OH groups. For three adsorbed water molecules, we see six frequencies (ranging from 4020 to 3041 cm^{-1}). Comparison of calculated and measured frequencies shows that lower water coverage is closer to the experimental system, as the number of peaks above 3500 cm^{-1} matches better, and the calculated frequencies are red-shifted with respect to the measured values.

3.7. Effect of Number of ALD Cycles on Zinc Loading.

Figure 9 shows zinc loading versus the number of ALD cycles. Here, one full cycle includes the $Zn(acac)_2$ reaction with ZrO_2, followed by removal of the ligand by air. The zinc loading increases with increasing ALD cycles up to three. After the first ALD cycle, zinc loading is ca. 1.2 wt %. The uptake of zinc loading decreases to 0.95 and 0.62 wt % in the second and third ALD cycle, respectively. The zinc loading was converted to the areal number density of zinc (nm^{-2}), assuming the mass gain from zinc addition and no change in the sample surface area between ALD cycles. The GPC of each cycle shown in nm^{-2} also decreased with an increasing number of ALD cycles.

3.8. XANES. The electronic structure of the zinc of the samples prepared with one-three ALD cycles was analyzed using XANES. Figure 10 shows the Zn K-edges of the ALD samples and Zn metal, bulk ZnO (wurtzite), and $Zn(acac)_2$ as references. The XANES spectrum of the Zn metal is a reference standard, using which the energy axis is calibrated so that the peak of its first derivative (inflection point) is at 9.659 keV. The most obvious information from XANES related to the oxidation state and the local coordination geometry. The XANES spectra of ZnO (wurtzite) and $Zn(acac)_2$ reference are rather similar, with the main edge peak at 9.669 keV, and they represent spectra of tetrahedrally coordinated Zn^{2+}. The

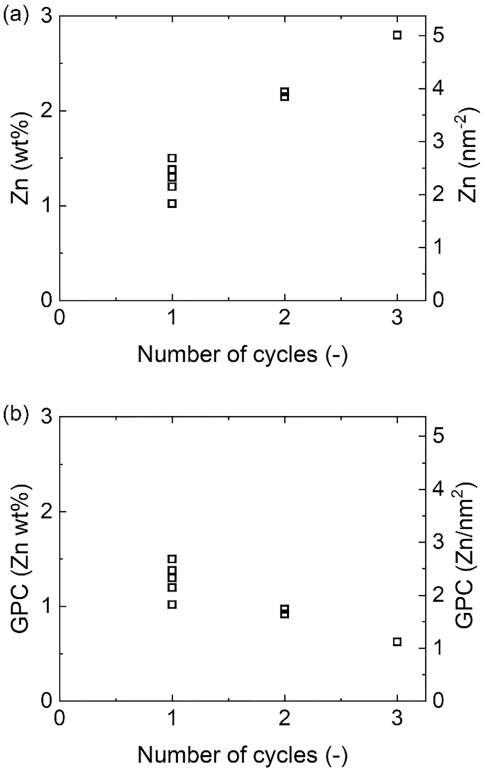

Figure 9. Controlling the zinc loading on ZrO_2 by repeating the $Zn(acac)_2$ ALD process. One ALD cycle comprises the reaction of $Zn(acac)_2$ with ZrO_2, followed by ligand removal by air at 500 °C. (a) Zinc loading on ZrO_2 after each cycle and (b) GPC (wt % and nm^{-2}) of the ALD process.

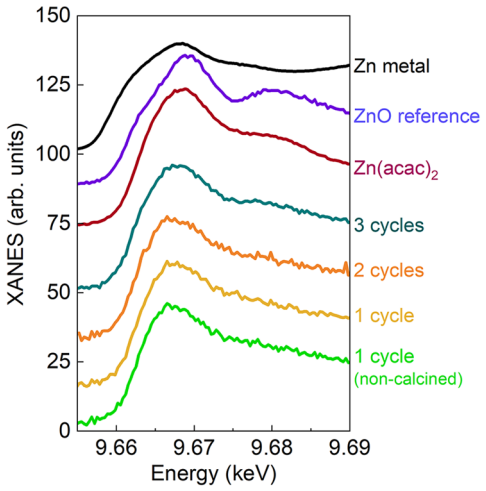

Figure 10. Zn K-edge XANES spectra for different numbers of $Zn(acac)_2$ ALD cycles. The XANES spectra of the $Zn(acac)_2$ reactant, wurtzite ZnO, and Zn metal are included as references.

XANES spectra of samples with different numbers of ALD cycles are very similar, with a slight difference to the Zn^{2+} references that their main peak has slightly shifted toward lower energies, to 9.667 keV. Similar behavior is observed in nanoscale Zn^{2+} oxides.[102] Otherwise, overall, all their spectra resemble the peaks of Zn^{2+} in the spectra of the $Zn(acac)_2$ reference, having somewhat broader features than those of the crystalline ZnO (wurtzite) reference. We can conclude that the

https://doi.org/10.1021/acs.chemmater.3c00668
Chem. Mater. XXXX, XXX, XXX−XXX

zinc species in our samples are present as Zn^{2+} and are independent of the number of ALD cycles.

3.9. XPS Analysis. The elemental composition of samples prepared with one to three ALD cycles was determined by XPS. Table 2 shows the elemental composition and relative amounts of different zinc components. The surface concentration of zinc increases from ca. 3.8 to 5.2 atom %, while that of zirconia decreases with increasing ALD cycle numbers. Zinc was in the Zn^{2+} state in all samples. The maximum of the Zn $2p_{3/2}$ peak appears at a binding energy of approximately 1021.8 eV, and the $L_3M_{45}M_{45}$ Auger peak appears at a kinetic energy of 987.7 eV, giving a modified Auger parameter of approximately 2009.5 eV, which corresponds well with the expected literature value.[103] Shifts in the binding energy of the $2p_{3/2}$ peak are generally rather small for different chemical states of Zn, but a broadening of the peak and appearance of a shoulder at higher binding energies can be generally attributed to the presence of several different chemical species. The Zn $2p_{3/2}$ peak was deconvoluted into three components at binding energies of 1021.5, 1023.1, and 1024.4 eV, most likely corresponding to ZnO and two different zinc mixed-oxide states a and b, respectively (Figure S10). The total concentration of the zinc mixed states a and b increases with increasing zinc loading. The maximum intensity of the O 1s peak appears at approximately 529.9 eV, with a considerable shoulder in the peak appearing at a higher binding energy. The peak was deconvoluted using three Gaussian components at approximately 529.8, 531.2, and 532.5 eV. These peaks were attributed to lattice oxygen in ZrO_2, oxygen in sub- or mixed-oxides, and surface hydroxyls, respectively. Most of the oxygen was found to be lattice oxygen in ZrO_2 (Table S2). According to this analysis, the concentration of hydroxyls decreases with increasing ALD cycle numbers.

Table 2. Relative Concentration of Elements and Different Components of Zinc in the Samples with Different ALD Cycle Numbers Determined via XPS

	elemental composition (atom %)					relative components of zinc (%)	
ALD cycle number	Zn 2p	Zr 3d	O 1s	F 1s	C 1s	ZnO	Zn mixed state a + b
0	0.0	32.4	55.1	1.6	10.9		
1	3.8	29.7	54.5	2.1	9.9	78.2	20.6 + 1.1
2	4.6	29.4	51.3	1.9	12.8	72.2	23.2 + 4.6
3	5.2	29.2	52.0	2.2	11.5	71.0	28.2 + 0.8

3.10. LEIS Analysis. LEIS measurements were performed to determine the relative surface area of ZnO from different ALD cycle number samples along with bare ZrO_2 calcined at 600 °C. In addition, a pure ZnO powder sample was analyzed as a Zn reference. The 3 keV He^+ spectra in Figure 11a allow detection of all elements heavier than 10 Da, that is, carbon and heavier elements. Only the expected surface peaks for O, Zn, and Zr were detected, indicating the absence of any impurities. Surface peak areas are proportional to the surface fraction of the respective elements. Figure 11b shows 5 keV Ne^+ spectra. Only elements heavier than Ne were detected. In these spectra, the Zn and Zr peaks are properly separated, and peak areas are easily evaluated by subtracting the baseline.

The results are summarized in Table 3. Assuming that the pure ZnO sample is a suitable reference, the surface fraction of ZnO after a single ALD cycle is quantified as 35%. With additional ALD cycles, the surface fraction of ZnO only slightly increases up to 39%. Thus, the initial ALD cycle leads to a good surface fraction of ZnO. The additional ZnO added during the second and third cycles is mostly located on the existing ZnO phase from the first cycle. Decreasing LEIS signal of Zr with increasing ALD cycle numbers indicates that some extent of ZnO was added on unoccupied reactive sites of ZrO_2.

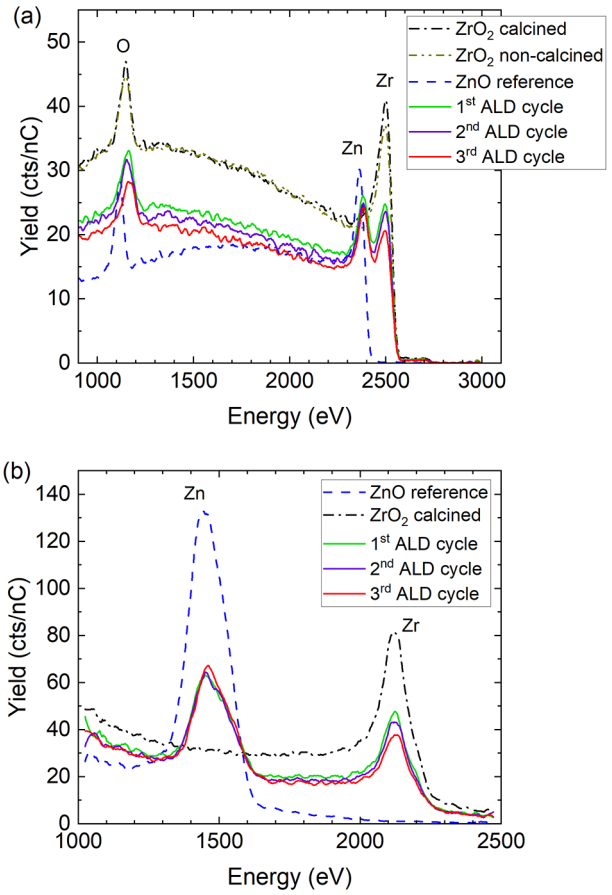

Figure 11. LEIS spectra of ZnO ALD samples deposited on ZrO_2 with different ALD cycle numbers. (a) 3 keV He^+ and (b) 5 keV Ne^+ were used as the primary ions. The LEIS spectra of the nontreated ZrO_2, ZrO_2 calcined at 600 °C, and ZnO powder as references. In 5 keV Ne^+ spectra, only elements heavier than Ne are detected, but the mass resolution is vastly improved compared to the He^+ spectra.

Table 3. Summary of the LEIS Results

sample	Zn intensity (cts/nC)	Zr intensity (cts/nC)	surface fraction of ZnO[a] (%)
ALD 1st cycle	5830	4620	35
ALD 2nd cycle	6150	4300	37
ALD 3rd cycle	6540	3700	39
ZnO reference	15830	0	100

[a]Quantified by comparison to ZnO reference.

4. DISCUSSION

4.1. Factors Affecting the Amount of Zinc Added by ALD. In this work, we investigated the effect of the ALD temperature and calcination temperature of the support on the

https://doi.org/10.1021/acs.chemmater.3c00668
Chem. Mater. XXXX, XXX, XXX−XXX

Table 4. Areal Number Density of Zinc Obtained in This Work Using $Zn(acac)_2$ Compared to That of Other Studies That Use Other Zinc Sources

support	BET surface area[a] ($m^2\ g^{-1}$)	zinc source (reactant A)	oxygen source (reactant B)	ALD temp (°C)	no. of cycles (−)	zinc loading (wt %)	GPC (nm)	GPC as Zn/nm^2	ref
porous ZrO_2	53.5	$Zn(acac)_2$	synthetic air	200	1	1.2		2.2	this work
porous ZrO_2	53.5	$Zn(acac)_2$	synthetic air	220	1	1.3		2.3	this work
porous ZrO_2	53.5	$Zn(acac)_2$	synthetic air	240	1	1.7		3.0	this work
porous ZrO_2	70.0	$Zn(acac)_2$	synthetic air	200	1	1.4		1.9	55
porous CuO/ZrO_2		$Zn(acac)_2$	synthetic air	200	1	1.1		1.5	55
porous Cu/SiO_2	264	DEZ	H_2O	150	1	1.5		0.5	54
HZSM-5 zeolite	320	DEZ	H_2O	120	1	5.8		1.8	47
HZSM-5 zeolite	432	DMZ	H_2O	210	50	0.01[b]		0.002[b]	46
HY zeolite	532	DEZ	H_2O	120	1	11.9		2.4	47
porous SiO_2	505	DEZ	H_2O	80	1	12.0		2.1	14
porous SiO_2	505	DEZ	H_2O	80	1	16.1		2.8	13
$Cu(OH)_2$ nanowire		DEZ	H_2O	50	20		0.19	7.9	106
Si(100)		DEZ	H_2O	150	250[c]		0.25	10.4	69
Si(100)		DEZ	H_2O	70−200			0.19	7.9	107
Si(100)		DMZ	H_2O	150	300[c]		0.28	11.6	69
Si wafer		DEZ	H_2O	150	100		0.20	8.3	108
glass		DEZ	H_2O	105−165	1600[d]		0.28[d]	11.6	104
glass		DEZ	H_2O	130−170	200		0.13	5.4	70
glass		DMZ	H_2O	120−170	300		0.14	5.8	70
sapphire(0001)		$Zn(OAc)_2$	H_2O	350	100		0.30	12.4	67
sapphire(0001)		$Zn(OAc)_2$	H_2O	350	250		0.24	10.0	67
sapphire(0001)		$ZnCl_2$	O_2	450−550	200		0.26	10.8	72
GaN/Al_2O_3		$ZnCl_2$	O_2	480	4000		0.050	2.1	73

[a]BET surface area of supports before the addition of zinc. [b]The total zinc loading (wt %) was calculated from the ZnO content of 0.59 wt %.[46] The GPC (wt %) was estimated by dividing the total loading by 50 cycles. [c]The number of cycles was determined from Figure 1 in ref 69. [d]The number of cycles and GPC (nm) were determined from Figures 3 and 2 in ref 104, respectively.

zinc loading on mesoporous monoclinic ZrO_2 in one ALD cycle using $Zn(acac)_2$ and synthetic air. Approximately a constant zinc loading is obtained up to an ALD temperature of 200 °C, after which the loading slightly increases with increasing ALD temperature (Figure 4). This increase in zinc loading may indicate a change in favorable adsorption sites or reaction pathways at an elevated temperature or slight decomposition of $Zn(acac)_2$.[5,82] TG analysis (Figure 1) confirms the partial decomposition of the $Zn(acac)_2$ reactant at 240 °C. However, no color change is observed in samples formed at different ALD temperatures, and zinc loadings are rather uniform in different parts of the powder bed. These results suggest only a minor effect of $Zn(acac)_2$ decomposition at 240 °C. DRIFTS results support this idea: the spectrum of the 240 °C sample shows bands similar to those of the 200 °C sample, indicating that decomposition of $Zn(acac)_2$ barely occurs under our reaction conditions. With an increase in ALD cycle numbers up to three, the zinc loading (wt %) increases, while the GPC slightly decreases (Figure 9). This result suggests a substrate-enhanced growth[5] at least in the first ALD cycle: the GPC on the starting surface, ZrO_2, was slightly higher than on ZnO-modified ZrO_2. Meanwhile, the zinc loading (wt %) decreases with increasing calcination temperature of ZrO_2, as shown in Figure 5. This decrease in zinc loading is mainly due to the decrease of the ZrO_2 specific surface area from 99.2 to 14.5 $m^2\ g^{-1}$. Interestingly, the areal number density of zinc remains constant at ca. 2 nm^{-2}.

Table 4 presents the areal number density of zinc deposited via the $Zn(acac)_2$ reaction at 200 °C compared to various ALD processes reported earlier. The zinc areal number density values were calculated from data given in the publications using eqs 2 and 3. Interestingly, the areal number density of zinc reported in this article (2.2 nm^{-2}) is similar to that of zinc deposited on high surface area porous supports via the DEZ reaction,[13,47,14] except for one study that reported a relatively low areal number density of zinc (ca. 0.5 nm^{-2}) via the DEZ reaction with a Cu/SiO_2 support.[54] A study on the ZnO ALD on HZMS-5 zeolite with DMZ and water also reported a rather low GPC value (ca. 0.01 wt %).[46] When the same DEZ reactant was used as the zinc source for coating nonporous planar substrates, the areal number density of zinc tends to be significantly higher than that of zinc deposited on porous supports. A study with the DEZ reaction on glass reported a GPC value of 0.28 nm,[104] which gives an areal number density of zinc of 11.6 nm^{-2} (eq 3). This value is higher than a typical GPC value of <5 nm^{-2} for ALD[5,105] and close to the areal number density of zinc for an average bulk monolayer of 12.0 nm^{-2} (eq 4).

In conclusion, a rather wide range of areal number densities of zinc (0.002−12.4 nm^{-2}) has been reported in the literature for ZnO ALD processes. The areal number density of zinc obtained in this work (2.2−3.0 nm^{-2}) is in the middle of this range and comparable to that obtained on porous supports via the DEZ reaction.

https://doi.org/10.1021/acs.chemmater.3c00668
Chem. Mater. XXXX, XXX, XXX−XXX

Table 5. Summary of the Elemental Analysis of Materials Deposited via ALD with Various Metal Acetylacetonate Reactants

$M(acac)_n$ reactant	n in $M(acac)_n$	support	pretreatment temp (°C)	reaction temp (°C)	metal atoms (nm^{-2})	acac ligands (nm^{-2})	acac/metal ratio after adsorption	ref
$Zn(acac)_2$	2	ZrO_2	600	200	2.2	1.8	0.8	this work
$Ni(acac)_2$	2	Al_2O_3	200	200	2.4	2.4	1.0[a]	38
$Co(acac)_3$	3	Al_2O_3	600	180	1.5	2.6	1.7	110
$Cr(acac)_3$	3	Al_2O_3	600	200	0.8	1.8[b]	2.2[b]	109
$Cr(acac)_3$	3	SiO_2	200	200	0.8	1.6	2.0	99
$Ir(acac)_3$	3	Al_2O_3	200	200	0.7[c]	1.8[c]	2.6	111
$Ir(acac)_3$	3	Al_2O_3	200	250	0.9[c]	1.9[c]	2.1	111
$Ir(acac)_3$	3	SiO_2	200	250	0.6[c]	0.7[c]	1.2	111
$Ir(acac)_3$	3	SiO_2–Al_2O_3	200	200	0.7[c]	1.6[c]	2.3	111
$Ir(acac)_3$	3	SiO_2–Al_2O_3	200	250	1.1[c]	1.5[c]	1.4	111

[a]The acac/metal ratio was estimated from the C/Ni ratio of 5 from the sample with Al_2O_3 preheated at 200 °C.[38] [b]The amount of acac ligands and acac/metal ratio were estimated from the C/Cr ratio of 11.[109] [c]The amount of acac ligands and Ir obtained were determined from Figure 2 in ref 111.

4.2. Distribution of Zinc within a ZrO_2 Particle. In SEM-EDS analysis of the sample prepared with one ALD cycle, zinc was present throughout the ZrO_2 particle (Figure 3). No accumulation of zinc at the edges of the zirconia particles was observed. This contrasts a recent study, where in addition to rather homogeneously distributed TiO_2 inside γ-Al_2O_3 particles, enrichment of TiO_2 was observed at the edges of the particles.[50]

The zinc intensity near the center was somewhat lower than that on the outer surface (Figure 3). In this work, we made a reference experiment to investigate the reaction of the Hacac byproduct with ZrO_2 (for details see the Experimental Section). Figure 6 shows the DRIFT spectrum of Hacac/ZrO_2 which is similar to those of the $Zn(acac)_2/ZrO_2$ sample and $Zn(acac)_2$ reference suggesting that Hacac, too, reacts with ZrO_2. As $Zn(acac)_2$ gets consumed during the reaction of $Zn(acac)_2$ with the ZrO_2 support, Hacac byproducts form and diffuse to the center of the ZrO_2 particles before the $Zn(acac)_2$ reactant, consuming reactive sites. DRIFTS and SEM-EDS results suggest that during the reaction of $Zn(acac)_2$ with ZrO_2, the competitive adsorption of Hacac on ZrO_2 might occur, decreasing the intensity of zinc inside the ZrO_2 particle.

4.3. Reaction Mechanism and Saturation-Determining Factor. In this section, we analyze the reaction mechanism of $Zn(acac)_2$ with ZrO_2 and compare it to earlier studies using other metal acetylacetonates [$M(acac)_n$]. The acac to metal ratios obtained by elemental analysis in this work and the literature are given in Table 5 (calculated from the carbon content by assuming one acetylacetonate ligand contains five carbon atoms). After adsorption via the ligand exchange reaction, one acac ligand from the $M(acac)_n$ reactant is released, leaving $n - 1$ ligands on the surface. In our samples prepared by using $Zn(acac)_2$ ($n = 2$), the ratio of acac to zinc is approximately 0.8. This ratio is close to one, indicating that at least one acac ligand is released into the gas phase during the $Zn(acac)_2$ reaction with the surface OH groups. Earlier ALD studies on other metal acetylacetonates have also reported the acac to metal ratio of ca. one for the $Ni(acac)_2$ reaction with Al_2O_3 and two for $Co(acac)_3$ and $Cr(acac)_3$ reactions with Al_2O_3 and SiO_2, resulting from the ligand exchange reaction.[38,99,109,110] Silvennoinen et al.[111] reported an acac to metal ratio of higher than two for the reaction of $Ir(acac)_3$ with Al_2O_3. They suggested that this ratio closed to three might have been caused by the competitive adsorption of Hacac byproducts on the Al_2O_3 surface or molecular associative adsorption.[111]

The amount of metal obtained by ALD can be defined by steric hindrance of bulky ligands.[5,82,83,99,112] Puurunen[83] demonstrated via a ball model that the GPC (nm^{-2}) decreases with increasing ligand size, and the GPC is typically less than 50% of a monolayer because of steric hindrance of ligands. Gu et al.[113] showed the effect of bulky reactants on areal coverage (%) by Monte Carlo simulations using various reactants such as trimethylaluminum (TMA) and dimethylaluminum isopropoxide (DMAI). The areal coverage of DMAI was lower than that of TMA because DMAI has a larger size. Li et al.[114] demonstrated using random sequential adsorption simulations that the surface density (nm^{-2}) covered by inhibitor molecules decreases with increasing radius of inhibitors. Lakomaa[4] reported 0.47 nm^2 as the filling area of one acac ligand. By taking the reciprocal of this filling area (eq 7 in ref 83), the theoretical maximum for the acac ligand packing can be estimated to be 2.1 nm^{-2}. Herein, the amount of acac ligands measured by carbon analysis (1.8 nm^{-2}) almost reached its theoretical maximum, suggesting that the steric hindrance of acac ligands acted as a saturation-determining factor.[5] Silvennoinen et al.[111] also concluded that steric hindrance is the saturation-determining factor[5] for the ligand exchange reaction of $Ir(acac)_3$ with Al_2O_3 because the amount of acac (1.6–1.9 nm^{-2}) is close to the maximum ligand packing value.

To support the idea that steric hindrance is the key to surface saturation, the areal number density of zinc was compared to the total number of surface OH groups. This work obtained ca. 2.2 nm^{-2} as the areal number density of zinc after one ALD cycle. Kouva et al.[92] reported ca. 6 nm^{-2} as the number of surface OH group on ZrO_2 calcined at 700 °C. Therefore, we can estimate the ratio of the amount of zinc atoms to that of surface OH groups to be approximately 0.4. This relatively low ratio likely indicates that the steric hindrance of acac ligands and not a limited number of OH groups defines surface saturation.

4.4. Growth Mode. The ZnO growth was studied by LEIS for samples prepared with up to three ALD cycles. LEIS results show the surface fraction of roughly one-third of ZnO after the first ALD cycle. This ZnO was well spread and acted as nuclei to cluster ZnO during the following ALD cycles. Thus, our

https://doi.org/10.1021/acs.chemmater.3c00668
Chem. Mater. XXXX, XXX, XXX–XXX

results indicate an two-dimensional growth mode during the first ALD cycle and island growth thereafter.[5]

Our results were compared to an earlier study by Jacobs et al.[39] on the NiO growth mode in the reaction of $Ni(acac)_2$ and ambient air with Al_2O_3. Jacobs et al.[39] performed ten ALD cycles and concluded that the Ni signal obtained by LEIS increases with increasing ALD cycles, but the rate of increase decreases after the first cycle. Meanwhile, the Ni XPS signal rather linearly increases. By comparing LEIS and XPS analyses, Jacobs et al.[39] concluded that atomically distributed Ni atoms obtained after the first ALD cycle acted as nuclei for the further cycles.[39] In conclusion, the ZnO ALD using $Zn(acac)_2$ and air shows a growth mode similar to that of the NiO ALD using $Ni(acac)_2$ and air.

5. CONCLUSIONS

This study investigated the deposition of ZnO on mesoporous high surface area ZrO_2 via ALD using $Zn(acac)_2$ and synthetic air and a fixed bed powder ALD reactor. The reaction of $Zn(acac)_2$ with ZrO_2 showed a saturating behavior. TG analysis showed good thermal stability of $Zn(acac)_2$ up to a temperature of ca. 240 °C. The areal number density of zinc had a constant value (ca. 2.2 nm^{-2}) with an increase in the amount of $Zn(acac)_2$. A similar value (ca. 2 nm^{-2}) was obtained on ZrO_2 calcined at various temperatures (400−1000 °C) with different surface areas (99.2−14.5 $m^2\ g^{-1}$). The elemental carbon and zinc analyses suggest that $Zn(acac)_2$ reacts with ZrO_2 most probably via ligand exchange with surface OH groups. This finding is supported by the DFT results, which further indicate the formation of zinc-bonded OH groups. Comparison to the literature indicates that the steric hindrance of acac ligands likely defines saturation. XANES and XPS analyses showed that zinc species are present as Zn^{2+}. The zinc loading in different parts of the powder bed was rather constant. However, SEM-EDS analysis revealed that the intensity of zinc near the center of a ZrO_2 particle was somewhat lower than that on the outer part of the particle. In-situ DRIFTS analysis shows that Hacac reacts with ZrO_2 suggesting the possible readsorption of some Hacac byproduct on the ZrO_2 surface, causing the lower intensity of zinc near the particle center. According to LEIS, the surface fraction of roughly one-third of ZnO was obtained from the first ALD cycle. In the following cycles, the already-deposited ZnO acted as a nucleation center for further ZnO growth. In conclusion, this study shows the potential of $Zn(acac)_2$ as an ALD reactant for coating high surface area porous ZrO_2 particles with ZnO.

■ ASSOCIATED CONTENT

Supporting Information

The Supporting Information is available free of charge at https://pubs.acs.org/doi/10.1021/acs.chemmater.3c00668.

Nitrogen physisorption isotherm of ZrO_2 calcined at various temperatures, photographs of samples inside the powder bed of the F-120 reactor and the tube furnace, thermal analysis of $Zn(acac)_2$, temperature program used for the in-situ DRIFTS-MS analysis, DRIFT spectra, XRD on ZrO_2, DFT calculations results, XPS spectra, a table for the relative amount of different components of oxygen determined by XPS, and nitrogen physisorption isotherm and physical properties of ZnO ALD samples (one and three ALD cycles) and nondecorated zirconia reference (PDF)

■ AUTHOR INFORMATION

Corresponding Author

Riikka L. Puurunen − *School of Chemical Engineering, Department of Chemical and Metallurgical Engineering, Aalto University, FI-00076 Aalto, Espoo, Finland;* orcid.org/0000-0001-8722-4864; Email: riikka.puurunen@aalto.fi

Authors

Jihong Yim − *School of Chemical Engineering, Department of Chemical and Metallurgical Engineering, Aalto University, FI-00076 Aalto, Espoo, Finland*

Eero Haimi − *School of Chemical Engineering, Department of Chemical and Metallurgical Engineering, Aalto University, FI-00076 Aalto, Espoo, Finland*

Miia Mäntymäki − *Department of Chemistry, University of Helsinki, 00014 Helsinki, Finland;* orcid.org/0000-0003-0880-0427

Ville Kärkäs − *School of Chemical Engineering, Department of Chemical and Metallurgical Engineering, Aalto University, FI-00076 Aalto, Espoo, Finland*

René Bes − *Department of Physics, University of Helsinki, 00014 Helsinki, Finland;* orcid.org/0000-0003-4206-1525

Aitor Arandia Gutierrez − *School of Chemical Engineering, Department of Chemical and Metallurgical Engineering, Aalto University, FI-00076 Aalto, Espoo, Finland*

Kristoffer Meinander − *School of Chemical Engineering, Department of Bioproducts and Biosystems, Aalto University, FI-00076 Aalto, Espoo, Finland*

Philipp Brüner − *IONTOF GmbH, 48149 Münster, Germany*

Thomas Grehl − *IONTOF GmbH, 48149 Münster, Germany*

Lars Gell − *Department of Chemistry, Nanoscience Center, University of Jyväskylä, FI-40014 Jyväskylä, Finland*

Tiia Viinikainen − *School of Chemical Engineering, Department of Chemical and Metallurgical Engineering, Aalto University, FI-00076 Aalto, Espoo, Finland*

Karoliina Honkala − *Department of Chemistry, Nanoscience Center, University of Jyväskylä, FI-40014 Jyväskylä, Finland;* orcid.org/0000-0002-3166-1077

Simo Huotari − *Department of Physics, University of Helsinki, 00014 Helsinki, Finland*

Reetta Karinen − *School of Chemical Engineering, Department of Chemical and Metallurgical Engineering, Aalto University, FI-00076 Aalto, Espoo, Finland*

Matti Putkonen − *Department of Chemistry, University of Helsinki, 00014 Helsinki, Finland;* orcid.org/0000-0002-4166-2890

Complete contact information is available at: https://pubs.acs.org/10.1021/acs.chemmater.3c00668

Author Contributions

J.Y. planned the experiments together with R.L.P., prepared the samples, made the physisorption measurements and XRD measurements, and performed DRIFTS-MS experiments together with T.V. and V.K. E.H. performed SEM-EDS analysis, M.M. the TG analysis, K.M. the XPS analysis, P.B. and T.G. the LEIS analysis, L.G. and K.H. the DFT calculations, and R.B. and S.M. the XANES analysis. J.Y. was responsible for writing the first version of the manuscript under the supervision of R.L.P. All the coauthors contributed to the final manuscript.

Funding

The work was financially supported by Prof. Puurunen's starting grant at Aalto University and by the Academy of Finland (COOLCAT consortium, decision no. 329977 and 329978; ALDI consortium, decision no. 331082; Matter and Materials, decision no. 318913 and decision no. 295696).

Notes

The authors declare no competing financial interest.

■ ACKNOWLEDGMENTS

Liliana Krotz and Walter Galotta are thanked for carbon content analysis. Hannu Revitzer is thanked for ICP-OES measurements. Joakim Kattelus is thanked for the standard deviation of ICP-OES measurements. Zahra Ahaliabadeh and Ville Miikkulainen are thanked for the design of the fixed bed reactor space for the F-120 reactor. This work made use of the Raw Materials Research Infrastructure and the ALD Center Finland Research Infrastructure. The University of Helsinki acknowledges the Center for X-ray Spectroscopy for providing experiment time and support with the HelXAS spectrometer under Proposal 2021-0011. The DFT calculations were made possible by computational resources provided by the CSC- IT Center for Science. The materials created in the Virtual Project on the History of ALD (VPHA) are acknowledged as a source of information on the early publications on ALD, including catalysis applications. Part of this work has been presented at the ALD 2022 conference, Ghent, Belgium, June 26−29, 2022.

■ REFERENCES

(1) Cremers, V.; Puurunen, R. L.; Dendooven, J. Conformality in Atomic Layer Deposition: Current Status Overview of Analysis and Modelling. *Applied Physics Reviews* **2019**, *6*, 021302.

(2) Haukka, S.; Kytökivi, A.; Lakomaa, E.-L.; Lehtovirta, U.; Lindblad, M.; Lujala, V.; Suntola, T. The utilization of saturated gas-solid reactions in the preparation of heterogeneous catalysts. *Stud. Surf. Sci. Catal.* **1995**, *91*, 957−966.

(3) Puurunen, R. L.; Root, A.; Sarv, P.; Viitanen, M. M.; Brongersma, H. H.; Lindblad, M.; Krause, A. O. I. Growth of Aluminum Nitride on Porous Alumina and Silica through Separate Saturated Gas−Solid Reactions of Trimethylaluminum and Ammonia. *Chem. Mater.* **2002**, *14*, 720−729.

(4) Lakomaa, E.-L. Atomic Layer Epitaxy (ALE) on Porous Substrates. *Appl. Surf. Sci.* **1994**, *75*, 185−196.

(5) Ommen, J. R.; Goulas, A.; Puurunen, R. L. Atomic layer deposition. In *Kirk-Othmer Encyclopedia of Chemical Technology*; John Wiley & Sons, Inc: New York, 2021; pp 1−42.

(6) Elam, J. W.; Routkevitch, D.; Mardilovich, P. P.; George, S. M. Conformal Coating on Ultrahigh-Aspect-Ratio Nanopores of Anodic Alumina by Atomic Layer Deposition. *Chem. Mater.* **2003**, *15*, 3507−3517.

(7) Gordon, R. G.; Hausmann, D.; Kim, E.; Shepard, J. A Kinetic Model for Step Coverage by Atomic Layer Deposition in Narrow Holes or Trenches. *Chem. Vap. Deposition* **2003**, *9*, 73−78.

(8) Libera, J. A.; Elam, J. W.; Pellin, M. J. Conformal ZnO Coatings on High Surface Area Silica Gel Using Atomic Layer Deposition. *Thin Solid Films* **2008**, *516*, 6158−6166.

(9) Yim, J.; Ylivaara, O. M. E.; Ylilammi, M.; Korpelainen, V.; Haimi, E.; Verkama, E.; Utriainen, M.; Puurunen, R. L. Saturation Profile Based Conformality Analysis for Atomic Layer Deposition: Aluminum Oxide in Lateral High-Aspect-Ratio Channels. *Phys. Chem. Chem. Phys.* **2020**, *22*, 23107−23120.

(10) Yim, J.; Verkama, E.; Velasco, J. A.; Arts, K.; Puurunen, R. L. Conformality of Atomic Layer Deposition in Microchannels: Impact of Process Parameters on the Simulated Thickness Profile. *Phys. Chem. Chem. Phys.* **2022**, *24*, 8645−8660.

(11) Feng, H.; Elam, J. W.; Libera, J. A.; Setthapun, W.; Stair, P. C. Palladium Catalysts Synthesized by Atomic Layer Deposition for Methanol Decomposition. *Chem. Mater.* **2010**, *22*, 3133−3142.

(12) Adomaitis, R. A. A Ballistic Transport and Surface Reaction Model for Simulating Atomic Layer Deposition Processes in High-Aspect-Ratio Nanopores. *Chem. Vap. Deposition* **2011**, *17*, 353−365.

(13) Ingale, P.; Knemeyer, K.; Piernavieja Hermida, M.; Naumann d'Alnoncourt, R.; Thomas, A.; Rosowski, F. Atomic Layer Deposition of ZnO on Mesoporous Silica: Insights into Growth Behavior of ZnO via In-Situ Thermogravimetric Analysis. *Nanomaterials* **2020**, *10*, 981.

(14) Knemeyer, K.; Baumgarten, R.; Ingale, P.; Naumann d'Alnoncourt, R.; Driess, M.; Rosowski, F. Toolbox for Atomic Layer Deposition Process Development on High Surface Area Powders. *Rev. Sci. Instrum.* **2021**, *92*, 025115.

(15) Szmyt, W.; Guerra-Nuñez, C.; Huber, L.; Dransfeld, C.; Utke, I. Atomic Layer Deposition on Porous Substrates: From General Formulation to Fibrous Substrates and Scaling Laws. *Chem. Mater.* **2022**, *34*, 203−216.

(16) Baumgarten, R.; Ingale, P.; Knemeyer, K.; Naumann d'Alnoncourt, R.; Driess, M.; Rosowski, F. Synthesis of High Surface Area—Group 13—Metal Oxides via Atomic Layer Deposition on Mesoporous Silica. *Nanomaterials* **2022**, *12*, 1458.

(17) Dendooven, J.; Deduytsche, D.; Musschoot, J.; Vanmeirhaeghe, R. L.; Detavernier, C. Modeling the Conformality of Atomic Layer Deposition: The Effect of Sticking Probability. *J. Electrochem. Soc.* **2009**, *156*, P63.

(18) Yanguas-Gil, A.; Elam, J. W. Simple Model for Atomic Layer Deposition Precursor Reaction and Transport in a Viscous-Flow Tubular Reactor. *Journal of Vacuum Science & Technology A: Vacuum, Surfaces, and Films* **2012**, *30*, 01A159.

(19) Keuter, T.; Menzler, N. H.; Mauer, G.; Vondahlen, F.; Vaßen, R.; Buchkremer, H. P. Modeling Precursor Diffusion and Reaction of Atomic Layer Deposition in Porous Structures. *Journal of Vacuum Science & Technology A: Vacuum, Surfaces, and Films* **2015**, *33*, 01A104.

(20) Ylilammi, M.; Ylivaara, O. M. E.; Puurunen, R. L. Modeling Growth Kinetics of Thin Films Made by Atomic Layer Deposition in Lateral High-Aspect-Ratio Structures. *J. Appl. Phys.* **2018**, *123*, 205301.

(21) Arts, K.; Vandalon, V.; Puurunen, R. L.; Utriainen, M.; Gao, F.; Kessels, W. M. M.; Knoops, H. C. M. Sticking Probabilities of H_2O and $Al(CH_3)_3$ during Atomic Layer Deposition of Al_2O_3 Extracted from Their Impact on Film Conformality. *Journal of Vacuum Science & Technology A* **2019**, *37*, 030908.

(22) Heikkinen, N.; Lehtonen, J.; Keskivali, L.; Yim, J.; Shetty, S.; Ge, Y.; Reinikainen, M.; Putkonen, M. Modelling Atomic Layer Deposition Overcoating Formation on a Porous Heterogeneous Catalyst. *Phys. Chem. Chem. Phys.* **2022**, *24*, 20506−20516.

(23) Zaera, F. Nanostructured Materials for Applications in Heterogeneous Catalysis. *Chem. Soc. Rev.* **2013**, *42*, 2746−2762.

(24) Lu, J.; Elam, J. W.; Stair, P. C. Synthesis and Stabilization of Supported Metal Catalysts by Atomic Layer Deposition. *Acc. Chem. Res.* **2013**, *46*, 1806−1815.

(25) Puurunen, R. L. A Short History of Atomic Layer Deposition: Tuomo Suntola's Atomic Layer Epitaxy. *Chem. Vap. Deposition* **2014**, *20*, 332−344.

(26) O'Neill, B. J.; Jackson, D. H. K.; Lee, J.; Canlas, C.; Stair, P. C.; Marshall, C. L.; Elam, J. W.; Kuech, T. F.; Dumesic, J. A.; Huber, G. W. Catalyst Design with Atomic Layer Deposition. *ACS Catal.* **2015**, *5*, 1804−1825.

(27) Lu, J. (Invited) Atomic Layer Deposition for Catalyst "Bottom-up" Synthesis. *ECS Trans.* **2016**, *75*, 85−92.

(28) Alvaro, E.; Yanguas-Gil, A. Characterizing the Field of Atomic Layer Deposition: Authors, Topics, and Collaborations. *PLoS One* **2018**, *13*, No. e0189137.

(29) Lu, J. Atomic Lego Catalysts Synthesized by Atomic Layer Deposition. *Acc. Mater. Res.* **2022**, *3*, 358−368.

(30) Malygin, A. A.; Malkov, A. A.; Dubrovenskii, S. D. Chapter 1.8 The chemical basis of surface modification technology of silica and

https://doi.org/10.1021/acs.chemmater.3c00668
Chem. Mater. XXXX, XXX, XXX−XXX

alumina by molecular layering method. *Stud. Surf. Sci. Catal.* **1996**, *99*, 213−236.
(31) Malygin, A. A.; Drozd, V. E.; Malkov, A. A.; Smirnov, V. M. From V. B. Aleskovskii's "Framework" Hypothesis to the Method of Molecular Layering/Atomic Layer Deposition. *Chem. Vap. Deposition* **2015**, *21*, 216−240.
(32) Suntola, T.; Antson, J. Method for producing compound thin films, International patent, FIN 52359, US 4 058 430, priority Nov 29, 1974, publication Nov 15, 1977.
(33) Suntola, T. Atomic Layer Epitaxy. *Mater. Sci. Rep.* **1989**, *4*, 261−312.
(34) Lakomaa, E.-L.; Lindblad, M.; Kytökivi, A.; Siro-Minkkinen, H.; Haukka, S. In *Catalysis in Finland - an exciting pathway*; Suomen Katalyysiseura: 2013; pp 93−103.
(35) Damyanov, D. *Growth by molecular layering of a catalytically active phase on the oxide surfaces, habilitation thesis*; Burgas Institute of Technology: 1988 (in Bulgarian).
(36) Suntola, T.; Lakomaa, E.-L.; Knuuttila, H.; Knuuttila, P.; Krause, O.; Lindfors, S. Process and apparatus for preparing heterogenous catalysts, International patent, FIN 900252, US 6 534 431, priority Jan 16, 1990, publication Mar 18, 2003.
(37) Suntola, T.; Haukka, S.; Kytökivi, A.; Lakomaa, E.-L.; Lindblad, M.; Hietala, J.; Hokkanen, H.; Knuuttila, H.; Knuuttila, P.; Krause, O.; et al. Method for preparing heterogeneous catalysts of desired metal content, FI 913438, EP 0 525 503 B1, priority Jul 16, 1991, publication Mar 10, 1999.
(38) Lindblad, M.; Lindfors, L. P.; Suntola, T. Preparation of Ni/Al2O3 Catalysts from Vapor Phase by Atomic Layer Epitaxy. *Catal. Lett.* **1994**, *27*, 323−336.
(39) Jacobs, J.-P.; Lindfors, L. P.; Reintjes, J. G. H.; Jylhä, O.; Brongersma, H. H. The Growth Mechanism of Nickel in the Preparation of Ni/Al2O3 Catalysts Studied by LEIS, XPS and Catalytic Activity. *Catal. Lett.* **1994**, *25*, 315−324.
(40) Knuuttila, H.; Lakomaa, E.-L. Polymerization catalyst for olefines, US 5 290 748 A, priority Jan 16, 1990, publication Mar 1, 1994.
(41) Volkova, A. N.; Malygin, A. A.; Koltsov, S. I.; Aleskovskii, V. B. The method of synthesis of Cr(III) and P(V) oxide layers on the silicagel surface, USSR author's certificate 422446, April 5, 1974 (in Russian).
(42) Malygin, A. A.; Volkova, A. N.; Kol'tsov, S. I.; Aleskovskii, V. B. The method of synthesis of vanadium oxide catalyst for the oxidation of organic compounds, USSR author's certificate 422447, April 5, 1974 (in Russian).
(43) Damyanov, D.; Velikova, M.; Ivanov, Iv.; Vlaev, L. On the Mechanism of Interaction between TiCl4 Vapour and Surface OH Groups of Amorphous SiO_2. *J. Non-Cryst. Solids* **1988**, *105*, 107−113.
(44) Lu, J.; Fu, B.; Kung, M. C.; Xiao, G.; Elam, J. W.; Kung, H. H.; Stair, P. C. Coking- and Sintering-Resistant Palladium Catalysts Achieved Through Atomic Layer Deposition. *Science* **2012**, *335*, 1205−1208.
(45) Gould, T. D.; Lubers, A. M.; Neltner, B. T.; Carrier, J. V.; Weimer, A. W.; Falconer, J. L.; Will Medlin, J. Synthesis of Supported Ni Catalysts by Atomic Layer Deposition. *J. Catal.* **2013**, *303*, 9−15.
(46) Wang, F.; Xiao, W. Y.; Xiao, G. M. Atomic Layer Deposition of Zinc Oxide on HZSM-5 Template and Its Methanol Aromatization Performance. *Catal. Lett.* **2015**, *145*, 860−867.
(47) Gong, T.; Qin, L.; Lu, J.; Feng, H. ZnO Modified ZSM-5 and Y Zeolites Fabricated by Atomic Layer Deposition for Propane Conversion. *Phys. Chem. Chem. Phys.* **2016**, *18*, 601−614.
(48) Ingale, P.; Knemeyer, K.; Preikschas, P.; Ye, M.; Geske, M.; Naumann d'Alnoncourt, R.; Thomas, A.; Rosowski, F. Design of PtZn Nanoalloy Catalysts for Propane Dehydrogenation through Interface Tailoring *via* Atomic Layer Deposition. *Catal. Sci. Technol.* **2021**, *11*, 484−493.
(49) Strempel, V. E.; Löffler, D.; Kröhnert, J.; Skorupska, K.; Johnson, B.; d'Alnoncourt, R. N.; Driess, M.; Rosowski, F. Enhancing of Catalytic Properties of Vanadia via Surface Doping with Phosphorus Using Atomic Layer Deposition. *Journal of Vacuum Science & Technology A: Vacuum, Surfaces, and Films* **2016**, *34*, 01A135.
(50) Moulijn, J. A.; Van Ommen, J. R.; Goulas, A.; Valdesueiro, D.; Juan-Alcañiz, J.; Au-Yeung, K.-M.; Woning, L.; Bergwerff, J. A. Synthesis of Highly-Uniform Titania Overcoats on a Mesoporous Alumina Catalyst Support by Atomic Layer Deposition and Their Application in Hydroprocessing. *Catal. Sci. Technol.* **2023**, *13*, 3537.
(51) Ingale, P.; Guan, C.; Kraehnert, R.; Naumann d'Alnoncourt, R.; Thomas, A.; Rosowski, F. Design of an Active and Stable Catalyst for Dry Reforming of Methane via Molecular Layer Deposition. *Catal. Today* **2021**, *362*, 47−54.
(52) Ro, I.; Liu, Y.; Ball, M. R.; Jackson, D. H. K.; Chada, J. P.; Sener, C.; Kuech, T. F.; Madon, R. J.; Huber, G. W.; Dumesic, J. A. Role of the Cu-ZrO_2 Interfacial Sites for Conversion of Ethanol to Ethyl Acetate and Synthesis of Methanol from CO_2 and H_2. *ACS Catal.* **2016**, *6*, 7040−7050.
(53) Zhao, F.; Gong, M.; Cao, K.; Zhang, Y.; Li, J.; Chen, R. Atomic Layer Deposition of Ni on Cu Nanoparticles for Methanol Synthesis from CO_2 Hydrogenation. *ChemCatChem* **2017**, *9*, 3772−3778.
(54) Gao, J.; Boahene, P. E.; Hu, Y.; Dalai, A.; Wang, H. Atomic Layer Deposition ZnO Over-Coated Cu/SiO_2 Catalysts for Methanol Synthesis from CO_2 Hydrogenation. *Catalysts* **2019**, *9*, 922.
(55) Arandia, A.; Yim, J.; Warraich, H.; Leppäkangas, E.; Bes, R.; Lempelto, A.; Gell, L.; Jiang, H.; Meinander, K.; Viinikainen, T.; et al. Effect of Atomic Layer Deposited Zinc Promoter on the Activity of Copper-on-Zirconia Catalysts in the Hydrogenation of Carbon Dioxide to Methanol. *Appl. Catal. B: Environmental* **2023**, *321*, 122046.
(56) Haukka, S.; Lakomaa, E.-L.; Suntola, T. Adsorption controlled preparation of heterogeneous catalysts. *Stud. Surf. Sci. Catal.* **1999**, *120*, 715−750.
(57) Lashdaf, M.; Krause, A. O. I.; Lindblad, M.; Tiitta, M.; Venäläinen, T. Behaviour of Palladium and Ruthenium Catalysts on Alumina and Silica Prepared by Gas and Liquid Phase Deposition in Cinnamaldehyde Hydrogenation. *Appl. Catal. A: General* **2003**, *241*, 65−75.
(58) Saedy, S.; Newton, M. A.; Zabilskiy, M.; Lee, J. H.; Krumeich, F.; Ranocchiari, M.; van Bokhoven, J. A. Copper−Zinc Oxide Interface as a Methanol-Selective Structure in Cu−ZnO Catalyst during Catalytic Hydrogenation of Carbon Dioxide to Methanol. *Catal. Sci. Technol.* **2022**, *12*, 2703−2716.
(59) Hariskos, D.; Spiering, S.; Powalla, M. Buffer Layers in Cu(In,Ga)Se2 Solar Cells and Modules. *Thin Solid Films* **2005**, *480*−*481*, 99−109.
(60) Kattel, S.; Ramírez, P. J.; Chen, J. G.; Rodriguez, J. A.; Liu, P. Active Sites for CO_2 Hydrogenation to Methanol on Cu/ZnO Catalysts. *Science* **2017**, *355*, 1296−1299.
(61) Listewnik, P.; Hirsch, M.; Struk, P.; Weber, M.; Bechelany, M.; Jędrzejewska-Szczerska, M. Preparation and Characterization of Microsphere ZnO ALD Coating Dedicated for the Fiber-Optic Refractive Index Sensor. *Nanomaterials* **2019**, *9*, 306.
(62) Tynell, T.; Karppinen, M. Atomic Layer Deposition of ZnO: A Review. *Semicond. Sci. Technol.* **2014**, *29*, 043001.
(63) *Diethylzinc*; CAS No. 557-20-0 [Online]; Sigma-Aldrich: St. Louis, September 22, 2021. https://www.sigmaaldrich.com/FI/en/sds/aldrich/256781 (accessed 2022-10-20).
(64) Butcher, K. S. A.; Afifuddin; Chen, P. P.-T.; Godlewski, M.; Szczerbakow, A.; Goldys, E. M.; Tansley, T. L.; Freitas, J. A. Recrystallization Prospects for Freestanding Low-Temperature GaN Grown Using ZnO Buffer Layers. *J. Cryst. Growth* **2002**, *246*, 237−243.
(65) Kopalko, K.; Wójcik, A.; Godlewski, M.; Łusakowska, E.; Paszkowicz, W.; Domagała, J. Z.; Godlewski, M. M.; Szczerbakow, A.; Świątek, K.; Dybko, K. Growth by Atomic Layer Epitaxy and Characterization of Thin Films of ZnO. *phys. stat. sol. (c)* **2005**, *2*, 1125−1130.
(66) Tammenmaa, M.; Koskinen, T.; Hiltunen, L.; Niinistö, L.; Leskelä, M. Zinc Chalcogenide Thin Films Grown by the Atomic

https://doi.org/10.1021/acs.chemmater.3c00668
Chem. Mater. XXXX, XXX, XXX−XXX

Layer Epitaxy Technique Using Zinc Acetate as Source Material. *Thin Solid Films* **1985**, *124*, 125−128.
(67) Kobayashi, K.; Okudaira, S. Preparation of ZnO Films on Sapphire (0001) Substrates by Alternate Supply of Zinc Acetate and H_2O. *Chem. Lett.* **1997**, *26*, 511−512.
(68) Guziewicz, E.; Godlewski, M.; Krajewski, T.; Wachnicki, Ł.; Szczepanik, A.; Kopalko, K.; Wójcik-Głodowska, A.; Przeździecka, E.; Paszkowicz, W.; Łusakowska, E.; et al. ZnO Grown by Atomic Layer Deposition: A Material for Transparent Electronics and Organic Heterojunctions. *J. Appl. Phys.* **2009**, *105*, 122413.
(69) Tanskanen, J. T.; Bakke, J. R.; Pakkanen, T. A.; Bent, S. F. Influence of Organozinc Ligand Design on Growth and Material Properties of ZnS and ZnO Deposited by Atomic Layer Deposition. *Journal of Vacuum Science & Technology A: Vacuum, Surfaces, and Films* **2011**, *29*, 031507.
(70) Makino, H.; Miyake, A.; Yamada, T.; Yamamoto, N.; Yamamoto, T. Influence of Substrate Temperature and Zn-Precursors on Atomic Layer Deposition of Polycrystalline ZnO Films on Glass. *Thin Solid Films* **2009**, *517*, 3138−3142.
(71) Stepanova, N. A.; Smirnov, V. M.; Kol'tsov, S. I.; Aleskovskii, V. B. Study of the Reaction between Zinc Chloride and Silica Gel. *J. Appl. Chem. USSR* **1977**, *50*, 450.
(72) Kaiya, K.; Yoshii, N.; Omichi, K.; Takahashi, N.; Nakamura, T.; Okamoto, S.; Yamamoto, H. Atmospheric Pressure Atomic Layer Epitaxy of ZnO Using a Chloride Source. *Chem. Mater.* **2001**, *13*, 1952−1956.
(73) Kopalko, K.; Godlewski, M.; Domagala, J. Z.; Lusakowska, E.; Minikayev, R.; Paszkowicz, W.; Szczerbakow, A. Monocrystalline ZnO Films on GaN/Al_2O_3 by Atomic Layer Epitaxy in Gas Flow. *Chem. Mater.* **2004**, *16*, 1447−1450.
(74) Pilz, J.; Perrotta, A.; Christian, P.; Tazreiter, M.; Resel, R.; Leising, G.; Griesser, T.; Coclite, A. M. Tuning of Material Properties of ZnO Thin Films Grown by Plasma-Enhanced Atomic Layer Deposition at Room Temperature. *Journal of Vacuum Science & Technology A: Vacuum, Surfaces, and Films* **2018**, *36*, 01A109.
(75) Ali, A. A.; Hashim, A. M. Density Functional Theory Study of Atomic Layer Deposition of Zinc Oxide on Graphene. *Nanoscale Res. Lett.* **2015**, *10* (1), 299.
(76) Carra, C.; Dell'Orto, E.; Morandi, V.; Riccardi, C. ZnO Nanostructured Thin Films via Supersonic Plasma Jet Deposition. *Coatings* **2020**, *10*, 788.
(77) Haga, K.; Katahira, F.; Watanabe, H. Preparation of ZnO Films by Atmospheric Pressure Chemical-Vapor Deposition Using Zinc Acetylacetonate and Ozone. *Thin Solid Films* **1999**, *343−344*, 145−147.
(78) Brunauer, S.; Emmett, P. H.; Teller, E. Adsorption of Gases in Multimolecular Layers. *J. Am. Chem. Soc.* **1938**, *60*, 309−319.
(79) Barrett, E. P.; Joyner, L. G.; Halenda, P. P. The Determination of Pore Volume and Area Distributions in Porous Substances. I. Computations from Nitrogen Isotherms. *J. Am. Chem. Soc.* **1951**, *73*, 373−380.
(80) Honkanen, A.-P.; Ollikkala, S.; Ahopelto, T.; Kallio, A.-J.; Blomberg, M.; Huotari, S. Johann-Type Laboratory-Scale X-ray Absorption Spectrometer with Versatile Detection Modes. *Rev. Sci. Instrum.* **2019**, *90*, 033107.
(81) Fuller, M. P.; Griffiths, P. R. Diffuse Reflectance Measurements by Infrared Fourier Transform Spectrometry. *Anal. Chem.* **1978**, *50*, 1906−1910.
(82) Puurunen, R. L. Surface Chemistry of Atomic Layer Deposition: A Case Study for the Trimethylaluminum/Water Process. *J. Appl. Phys.* **2005**, *97*, 121301.
(83) Puurunen, R. L. Growth Per Cycle in Atomic Layer Deposition: A Theoretical Model. *Chem. Vap. Deposition* **2003**, *9*, 249−257.
(84) Blöchl, P. E. Projector Augmented-Wave Method. *Phys. Rev. B* **1994**, *50*, 17953−17979.
(85) Enkovaara, J.; Rostgaard, C.; Mortensen, J. J.; Chen, J.; Dułak, M.; Ferrighi, L.; Gavnholt, J.; Glinsvad, C.; Haikola, V.; Hansen, H. A.; et al. Electronic Structure Calculations with GPAW: A Real-Space Implementation of the Projector Augmented-Wave Method. *J. Phys.: Condens. Matter* **2010**, *22*, 253202.
(86) Wellendorff, J.; Lundgaard, K. T.; Møgelhøj, A.; Petzold, V.; Landis, D. D.; Nørskov, J. K.; Bligaard, T.; Jacobsen, K. W. Density Functionals for Surface Science: Exchange-Correlation Model Development with Bayesian Error Estimation. *Phys. Rev. B* **2012**, *85*, 235149.
(87) Dudarev, S. L.; Botton, G. A.; Savrasov, S. Y.; Humphreys, C. J.; Sutton, A. P. Electron-Energy-Loss Spectra and the Structural Stability of Nickel Oxide: An LSDA+U Study. *Phys. Rev. B* **1998**, *57*, 1505−1509.
(88) Korpelin, V.; Melander, M. M.; Honkala, K. Reducing the Irreducible: Dispersed Metal Atoms Facilitate Reduction of Irreducible Oxides. *J. Phys. Chem. C* **2022**, *126*, 933−945.
(89) Hjorth Larsen, A.; Jørgen Mortensen, J.; Blomqvist, J.; Castelli, I. E.; Christensen, R.; Dułak, M.; Friis, J.; Groves, M. N.; Hammer, B.; Hargus, C.; et al. The Atomic Simulation Environment—a Python Library for Working with Atoms. *J. Phys.: Condens. Matter* **2017**, *29*, 273002.
(90) Bitzek, E.; Koskinen, P.; Gähler, F.; Moseler, M.; Gumbsch, P. Structural Relaxation Made Simple. *Phys. Rev. Lett.* **2006**, *97*, 170201.
(91) Frederiksen, T.; Paulsson, M.; Brandbyge, M.; Jauho, A.-P. Inelastic Transport Theory from First Principles: Methodology and Application to Nanoscale Devices. *Phys. Rev. B* **2007**, *75*, 205413.
(92) Kouva, S.; Honkala, K.; Lefferts, L.; Kanervo, J. Review: Monoclinic Zirconia, Its Surface Sites and Their Interaction with Carbon Monoxide. *Catal. Sci. Technol.* **2015**, *5*, 3473−3490.
(93) Viinikainen, T.; Rönkkönen, H.; Bradshaw, H.; Stephenson, H.; Airaksinen, S.; Reinikainen, M.; Simell, P.; Krause, O. Acidic and Basic Surface Sites of Zirconia-Based Biomass Gasification Gas Clean-up Catalysts. *Appl. Catal. A: General* **2009**, *362*, 169−177.
(94) Voigt, P.; Haimi, E.; Lahtinen, J.; Cheah, Y. W.; Mäkelä, E.; Viinikainen, T.; Puurunen, R. L. Nickel Supported on Mesoporous Zirconium Oxide by Atomic Layer Deposition: Initial Fixed-Bed Reactor Study. *Top Catal* **2019**, *62*, 611−620.
(95) Korhonen, S. T.; Bañares, M. A.; Fierro, J. L. G.; Krause, A. O. I. Adsorption of Methanol as a Probe for Surface Characteristics of Zirconia-, Alumina-, and Zirconia/Alumina-Supported Chromia Catalysts. *Catal. Today* **2007**, *126*, 235−247.
(96) Hakuli, A.; Kytökivi, A. Binding of Chromium Acetylacetonate on a Silica Support. *Phys. Chem. Chem. Phys.* **1999**, *1*, 1607−1613.
(97) Nakamoto, K.; McCarthy, P. J.; Martell, A. E. Infrared Spectra of Metal Chelate Compounds. III. Infrared Spectra of Acetylacetonates of Divalent Metals. *J. Am. Chem. Soc.* **1961**, *83*, 1272−1276.
(98) Rautiainen, A.; Lindblad, M.; Backman, L. B.; Puurunen, R. L. Preparation of Silica-Supported Cobalt Catalysts through Chemisorption of Cobalt(Ii) and Cobalt(Iii) Acetylacetonate. *Phys. Chem. Chem. Phys.* **2002**, *4*, 2466−2472.
(99) Haukka, S.; Lakomaa, E.-L.; Suntola, T. Surface Coverage of ALE Precursors on Oxides. *Appl. Surf. Sci.* **1994**, *82−83*, 548−552.
(100) Kouva, S.; Andersin, J.; Honkala, K.; Lehtonen, J.; Lefferts, L.; Kanervo, J. Water and Carbon Oxides on Monoclinic Zirconia: Experimental and Computational Insights. *Phys. Chem. Chem. Phys.* **2014**, *16*, 20650−20664.
(101) Bazhenov, A. S.; Honkala, K. Understanding Structure and Stability of Monoclinic Zirconia Surfaces from First-Principles Calculations. *Top Catal* **2017**, *60*, 382−391.
(102) Perelshtein, I.; Ruderman, E.; Perkas, N.; Tzanov, T.; Beddow, J.; Joyce, E.; Mason, T. J.; Blanes, M.; Mollá, K.; Patlolla, A.; et al. Chitosan and Chitosan−ZnO-Based Complex Nanoparticles: Formation, Characterization, and Antibacterial Activity. *J. Mater. Chem. B* **2013**, *1*, 1968.
(103) Biesinger, M. C.; Lau, L. W. M.; Gerson, A. R.; Smart, R. St. C. Resolving Surface Chemical States in XPS Analysis of First Row Transition Metals, Oxides and Hydroxides: Sc, Ti, V, Cu and Zn. *Appl. Surf. Sci.* **2010**, *257*, 887−898.
(104) Yamada, A.; Sang, B.; Konagai, M. Atomic Layer Deposition of ZnO Transparent Conducting Oxides. *Appl. Surf. Sci.* **1997**, *112*, 216−222.

https://doi.org/10.1021/acs.chemmater.3c00668
Chem. Mater. XXXX, XXX, XXX−XXX

(105) Blomberg, T. (Invited) Unit Steps of an ALD Half-Cycle. *ECS Trans.* **2013**, *58*, 3−18.
(106) Liu, X.; Luo, J.; Wang, H.; Huang, L.; Wang, S.; Li, S.; Sun, Z.; Sun, F.; Jiang, Z.; Wei, S.; et al. In Situ Spectroscopic Characterization and Theoretical Calculations Identify Partially Reduced ZnO_{1-x}/Cu Interfaces for Methanol Synthesis from CO_2. *Angew. Chem. Int. Ed* **2022**, *61*, No. e202202330.
(107) Jeon, S.; Bang, S.; Lee, S.; Kwon, S.; Jeong, W.; Jeon, H.; Chang, H. J.; Park, H.-H. Structural and Electrical Properties of ZnO Thin Films Deposited by Atomic Layer Deposition at Low Temperatures. *J. Electrochem. Soc.* **2008**, *155*, H738.
(108) Min, Y.; An, C.; Kim, S.; Song, J.; Hwang, C. Growth and Characterization of Conducting ZnO Thin Films by Atomic Layer Deposition. *Bulletin of the Korean Chemical Society* **2010**, *31*, 2503−2508.
(109) Kytökivi, A.; Jacobs, J.-P.; Hakuli, A.; Meriläinen, J.; Brongersma, H. H. Surface Characteristics and Activity of Chromia/Alumina Catalysts Prepared by Atomic Layer Epitaxy. *J. Catal.* **1996**, *162*, 190−197.
(110) Haukka, S.; Lindblad, M.; Suntola, T. Growth Mechanisms of Mixed Oxides on Alumina. *Appl. Surf. Sci.* **1997**, *112*, 23−29.
(111) Silvennoinen, R. J.; Jylhä, O. J. T.; Lindblad, M.; Sainio, J. P.; Puurunen, R. L.; Krause, A. O. I. Atomic Layer Deposition of Iridium(III) Acetylacetonate on Alumina, Silica−Alumina, and Silica Supports. *Appl. Surf. Sci.* **2007**, *253*, 4103−4111.
(112) Suntola, T. Surface Chemistry of Materials Deposition at Atomic Layer Level. *Appl. Surf. Sci.* **1996**, *100−101*, 391−398.
(113) Gu, B.; Le Trinh, N.; Nguyen, C. T.; Yasmeen, S.; Gaiji, H.; Kang, Y.; Lee, H.-B.-R. Computational Modeling of Physical Surface Reactions of Precursors in Atomic Layer Deposition by Monte Carlo Simulations on a Home Desktop Computer. *Chem. Mater.* **2022**, *34*, 7635−7649.
(114) Li, J.; Tezsevin, I.; Merkx, M. J. M.; Maas, J. F. W.; Kessels, W. M. M.; Sandoval, T. E.; Mackus, A. J. M. Packing of Inhibitor Molecules during Area-Selective Atomic Layer Deposition Studied Using Random Sequential Adsorption Simulations. *Journal of Vacuum Science & Technology A* **2022**, *40*, 062409.

https://doi.org/10.1021/acs.chemmater.3c00668
Chem. Mater. XXXX, XXX, XXX−XXX